Estimation of the effective bone-elasticity tensor based on μCT imaging by a stochastic model. A multi-method validation

Davide Gagliardi[a], Vittorio Sansalone[a], Christophe Desceliers[b], Salah Naili[a],*

[a] Universiteé Paris-Est, Laboratoire Modelisation et Simulation Multi Echelle, MSME UMR 8208 CNRS, 61 avenue du Général de Gaulle, 94010 Créteil Cedex, France
[b] Universiteé Paris-Est, Laboratoire Modelisation et Simulation Multi Echelle, MSME UMR 8208 CNRS, 5, boulevard Descartes, 77454 Marne-la-Vallée, France

ARTICLE INFO

ABSTRACT

In previous work, we proposed a stochastic model to describe the elasticity of bone matrix (so-called ultra-structure, US) based on basic statistical information on the *tissue mineral density* (TMD). This information was obtained by analyzing high-resolution images of a human femoral neck realized by means of synchrotron radiation micro-computed tomography (SR − μCT). In this paper, we extend this study by focusing at the upper scale where cortical bone is described as a two-phase mixture made up of water-filled Haversian pores (HP) embedded in the surrounding solid US. The goal of this paper is to develop a stochastic model of cortical bone elasticity accounting for the effect of uncertainty affecting both phases, the US *via* the TMD and the HP.

Experimental information was assumed to be given in terms of mean values and dispersions of the average TMD (denoted $\overline{\text{TMD}}$) and HP at the millimeter scale. To this aim, SR − μCT images were used to extract several representative volume elements (RVEs) spanning the whole cortical tissue which, in turn, were analyzed to obtain the required statistical information on $\overline{\text{TMD}}$ and HP. This information has been used for constructing a stochastic multiscale model of cortical bone based on the Maximum Entropy (denoted MaxEnt) principle. This stochastic multiscale model is used in the estimation of the effective elastic properties of cortical bone (CB-SμM) based on continuum micromechanics (μM). In parallel, a deterministic nominal multiscale model of cortical bone (CB-NμM) was developed by using as input data the mean values of $\overline{\text{TMD}}$ and HP. The elastic *moduli* estimated with CB-NμM has been compared with the average value of the same counterpart obtained with the CB-SμM model. The two estimates differ for less than 1%, proving the robustness of the CB-NμM model to uncertainties. Moreover, the accuracy of the SμM stochastic model has been tested. Estimations of the cortical bone elasticity of each RVE with the μM (cylindrical HP and homogeneous US), has been compared with other estimation obtained through others homogenization techniques: *finite elements* (FEM) and *fast Fourier transform* (FFT), both able to account for the real morphology of Havesian porosity and the heterogeneity of the ultrastructure. Results show that (1) the transverse isotropic (TI) elastic μM model correctly approximates the FEM and FFT estimates (∼ 98% TI); (2) the μM model accurately estimates the axial *modulus* (Y_3) in longitudinal direction and the lateral contraction ratio ν_{31}.

1. Introduction

Assessment of mechanical properties of bone *in vivo* represents a challenging and complex problem because of the hierarchical and heterogeneous structure of bone material as well as for its capability to adapt its material properties to the superimposed mechanical and biochemical *stimuli* (Cowin, 2001).

Zooming from the organ scale down, bone elementary components (basically collagen, mineral, and water) give rise to different structural patterns. Aiming at predicting the overall behavior of bone, several methods have been proposed to account for this hierarchical structure such as homogenization methods (Crolet et al., 1993; Racila and Crolet, 2007; Parnell et al., 2011; Rohan et al., 2012) mean-field approximations (Parnell et al., 2011; Hellmich et al., 2004a), Finite Element (FE) numerical simulations (Barkaoui and Hambli, 2011, 2014) and many others.

All these methods require information about the constitutive relation, relative amount and spatial arrangement of the structural units at each scale considered in the description of bone. Although this information can be obtained *in vitro* using different techniques (mechanical testing, chemical analysis, imaging) with a relatively high level of accuracy, it is still challenging to access detailed information

---

about the microstructural organization of bone *in vivo*. Since reliability of model predictions rely on the accuracy of input data, the issue of dealing with uncertain data becomes of main importance in view of clinical applications. Moreover, in the framework of a computer-aided, patient-specific analysis, not only *accuracy* and *reliability* but also *simplicity* and *elaboration time* should be accounted for. In this context, it does make sense to develop a reliable, fast and easy-to-use model using minimal information about patient-specific bone microstructure.

Restricting our interest to modeling bone elasticity, analytical and semi-analytical methods often make use of a simplified description of bone in terms of morphology (structural units can be described by simple geometrical entities such as spheres, cylinders, ellipsoids, *etc.*) and elastic symmetry of its essential constituents (mineral is often modeled as an isotropic material, water as a compressible fluid, and collagen as either an isotropic or transversely isotropic material). Starting from these "universal" morphological and constitutive assumptions, the spatial heterogeneity of elastic properties of bone is described in terms of the relative amounts of its essential constituents. These approaches lead to relatively easy-to-use and time-efficient models which also proved to be accurate as long as input data (relative amount of bone constituents) are known. In this line, the relevance of modeling approaches capable to account for the specific composition and organization of bone constituents at each scale is apparent in Hellmich and Ulm (2002); Hellmich et al. (2004b, a); Fritsch and Hellmich (2007); Sansalone et al. (2010). However, being inherently deterministic in nature, these models cannot provide any clue about the reliability of their predictions nor on the effects of uncertainty possibly affecting the input data or the model assumptions.

As far as we know, the effects of uncertain morphology of bone microstructure has not been investigated so far. Recently, Sansalone et al. (2014) discussed the issue of uncertain elastic properties of bone constituents at the nanoscale and propagated this uncertainty upwards to quantify its effects on the elastic properties of the bone solid matrix (so-called ultrastructure, US). Another pretty unexplored issue concerns the interfaces between different structural units, which are commonly assumed to be in perfect adhesion.

The issue of bone composition, related to the spatial heterogeneity and distribution of bone, seems to have received more attention in the biomechanical community. For instance, it has been shown that bone mineralization density distribution (BMDD) is a reliable fingerprint of the health state of bone (Ruffoni et al., 2007). Assessing bone composition at microstructural scales requires experimental devices with suitable spatial resolution. In this context, X-ray based methods occupy a central place in clinics–where Dual-energy X-ray absorptiometry (DXA) is still the golden standard to diagnose and follow osteoporosis–as well as in research–where different types of micro-computed tomography (μCT) can be used to reveal tiny details of bone micro- and nano-structure. These methods can detect the attenuation of a radiative source due to the absorption of an interposed medium. In bone, attenuation is mostly due to the mineral whereas the contribution of collagen and water is much lower. In this work, this contribution is not taken into account. Synchrotron radiation μCT (SR $-$ μCT) is nowadays the more reliable technology to inspect bone morphology and composition at the micro- and nano-scale *in vitro* (Apostol et al., 2006; Langer et al., 2012). Last generation μCT devices also allow qualitative and quantitative assessment of bone at the micro-scale *in vitro* and, to a limited extent, *in vivo* (Burghardt et al., 2011). Due to X-ray dose limitations, *in vivo* human imaging has a spatial resolution limited to about one hundred micrometers and is restricted to analysis of structural parameters. These limitations make it impossible to obtain accurate information on bone composition at sub-millimeter scales *in vivo* and call for new modeling approaches capable to account for uncertain input data.

In Sansalone et al. (2016), a first proof of concept of the propagation of uncertainty was proposed. In this paper, we have started investigating the propagation of uncertainty related to bone composition through the scales. Adopting the simplified representation of bone proposed in Sansalone et al. (2010), uncertain bone composition was assumed to be known in terms of statistics (mean value and dispersion) of volume fractions (VFs) computed from experimental data at the scale of about ten micrometers. Uncertain VFs were modeled as random variables and their stochastic models were obtained by means of the Maximum Entropy (MaxEnt) principle. Eventually, random VFs were introduced in a micromechanical model to compute statistics of bone elastic *moduli* of the cortical bone. These statistics turned out to overestimate the actual elastic *moduli*. In a recent work (Sansalone et al., 2016), it was shown that the elastic coefficients of bone US are better represented by using the Tissue Mineral Density (TMD) to describe bone composition and using experimental data at the scale of several hundreds micrometers (that is, the size of the Representative Volume Element, RVE, of cortical bone). The average TMD at this scale was referred to as $\overline{\text{TMD}}$. In here, we aim at extending this analysis by investigating the propagation of uncertainty up to the tissue scale. Specifically, the stochastic model of US defined as TMD/RVE concept is combined with a stochastic model of the Haversian porosity (HP) in order to obtain a stochastic micromechanical model of the cortical bone.

The purpose of this work is manifold (*i*) to analyze the combined effect of the variations of the pair ($\overline{\text{TMD}}$, HP) on the elasticity of cortical bone; (*ii*) to validate the stochastic micromechanical model by comparison with more refined numerical models.

The first goal was achieved by using the pair ($\overline{\text{TMD}}$, HP) to describe bone composition. Both HP and $\overline{\text{TMD}}$ were modeled as statistically independent random variables and their probability density functions (PDFs) were obtained by means of the MaxEnt principle fed with experimental statistical information (mean value and dispersion) at the tissue scale. This information has been estimated by analyzing a set of RVEs issued from SR $-$ μCT images of the inferior femoral neck of an elderly patient. Eventually, the stochastic micromechanical model described in this work results from introducing this stochastic description of the pair ($\overline{\text{TMD}}$, HP) in the micromechanical model proposed by Sansalone et al. (2010).

The second goal was achieved by comparing the statistics of the elastic *moduli* of cortical bone predicted by the stochastic micromechanical model with the elastic *moduli* of actual RVEs computed using detailed microstructural models based on the Finite Element Method (μFE) (Crolet et al., 1993; Granke et al., 2015) and on the Fast Fourier Transform (μFFT) (Moulinec and Suquet, 1998; Brisard and Dormieux, 2010; Monchiet and Bonnet, 2012; Monchiet, 2015). Both these models can account for the actual pore morphology and heterogeneity of bone RVEs. which have been set up accounting the morphology of the Haversian porosity and the variability of the solid matrix existent in the reference μCT dataset.

After this introduction on the rationale for studying the estimations of bone elasticity, the paper is organized as follows. First, Sec. 2 describes the materials and methods employed in this study. The section starts with discussing our experimental data on bone composition and the related statistical information; then, an overview of some techniques providing the effective elastic properties of an heterogeneous material is presented, namely continuum micromechanics, FEM and FFT method. Eventually, several micromechanical and microstructural models of cortical bone elasticity are presented, including a new stochastic micromechanical model based on ($\overline{\text{TMD}}$, HP) is detailed. Then, Sec. 3 is devoted to describing the results obtained through all these models. The results of the stochastic model are presented first. The effects of the gray-level threshold chosen to separate HP from US in the SR $-$ μCT images are then investigated. Eventually, results of microstructural models based on the FEM and FFT method are presented and compared with those of the stochastic model. Finally, Sec. 4 draws the conclusions of this work and set the way ahead for future research.
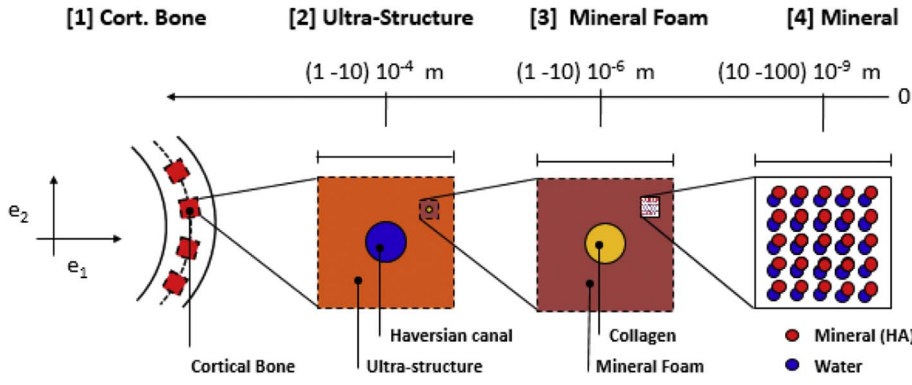
2. Material and methods

2.1. Hierarchical description of cortical bone

A four-scale description of cortical bone was proposed in (Sansalone et al., 2010). Below the organ scale, at the scale of several hundreds micrometers (tissue scale), cortical bone (CB) was considered as constituted of Haversian pores (HP) embedded in a solid matrix called ultrastructure (US). At the scale of a few tens micrometers (US scale), US was considered as made up of collagen (Col) fibers embedded in a mineral foam (MF). Eventually, at the scale of several tens nanometers (referred to as MF scale), MF was considered as a mixture of mineral (HA for Hydroxyapatite) and water (W). The model is depicted in Fig. 1.

2.2. Which information can be obtained on cortical bone from SR-μCT images?

Gray levels (GL) in μCT images are related to the linear attenuation coefficient (LAC) of the X-ray beam passing through an interposed medium. The LAC is the fraction of attenuated incident photons per unit thickness of a material. In bone, attenuation is in large part due to the mineral whereas the contribution of collagen and water is a lot weaker. In this work, this contribution is not taken into account. Therefore, the intensity of the LAC is related to the tissue mineral density (TMD) (see Fig. 2). An affine relationship exists between GL in SR-μCT images and TMD of bone, reading:

$$\mathrm{TMD} = \widehat{\mathrm{TMD}}(\mathrm{GL}) = c_0 + c_1 \times \mathrm{GL}, \tag{2.1}$$

where TMD designates the value of the affine function $\widehat{\mathrm{TMD}}(\mathrm{GL})$ for the value GL, coefficients c_0 and c_1 depend on the specific imaging device and have to be calibrated with respect to phantoms of known composition. In this study, our images were obtained using the beamline ID19 of the European Synchrotron Radiation Facility (ESRF,

Grenoble, France). SR-μCT measurements were performed according to the recommendations of Nuzzo et al. (2002): the X-ray beam energy was tuned to 25 keV – which provided the best signal-to-noise ratio in the study of Nuzzo and coworkers – and the voxel size was fixed at 10.13 μm – which was shown to be a good compromise between accuracy and field of view of the images (see Sansalone et al. (2010) for more details on the imaging procedure). After calibration, the coefficients c_0 and c_1 are given by:

$$c_0 = -\frac{0.5082}{3.319} \quad \text{and} \quad c_1 = \frac{5.5}{255 \times 3.319}. \tag{2.2}$$

By inspecting a typical SR-μCT image, it is possible to distinguish regions corresponding to Haversian porosity (HP) and ultrastructure (US). By fixing a threshold q for the GLs of the HP, the whole range of GLs, $\mathscr{GL} := [0,255]$, can be split into the ranges of GLs referring to HP and US voxels: $\mathscr{GL}_{\mathrm{HP}} := [0, q)$ and $\mathscr{GL}_{\mathrm{US}} := [q, 255]$, respectively. Then, two pieces of information are embedded in quantitative μCT images, *i.e.* the mineralization of the ultrastructure obtained through Eq. (2.1) and the value of the HP (relative number of voxels having a GL given by gl_i in $\mathscr{GL}_{\mathrm{HP}}$):

$$\mathrm{HP} = \frac{\sum_i \mathbb{1}_{\mathscr{GL}_{\mathrm{HP}}}(gl_i)}{\sum_i \mathbb{1}_{\mathscr{GL}}(gl_i)}, \tag{2.3}$$

where $\mathbb{1}_{\mathcal{I}}(x)$ represents the characteristic function of the set $\mathcal{I}$. The relation (2.3) is plotted on Fig. 2(c). This graph shows the gray-level occurrences which can be interpreted in the framework of the probability theory. So, the random variable GL associated with the gray-level is linked with the random variable HP through Eq. (2.1) which is approximated by the area under the PDF(GL) restricted to the domain GL $\leq q$, *i.e.* HP = $\mathbb{P}(\mathrm{GL} \leq q)$ where the notation $\mathbb{P}(\mathrm{GL} \leq q)$ designates the probability that GL $\leq q$.

It is worth noting that HP and TMD are defined at different scales. On the one side, HP is defined at the tissue scale and was measured on a RVE-wise basis (see inset (b) in Fig. 2 depicting a typical RVE is taken as
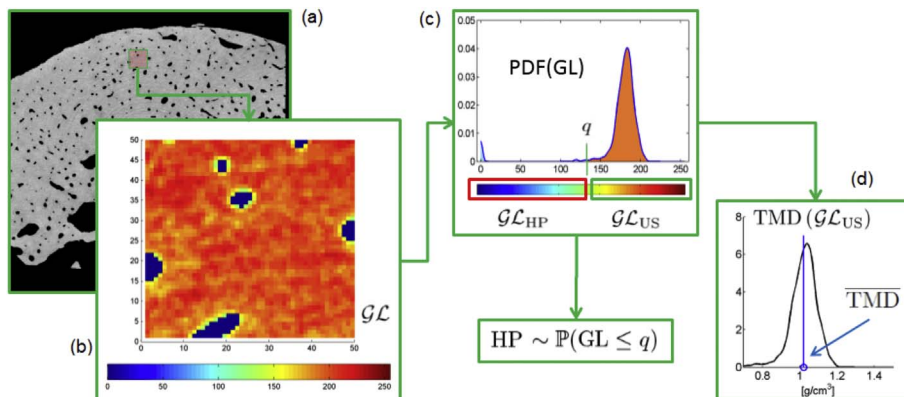

Fig. 2. Experimental information obtained from SR-μCT images. (a) Typical graylevel cross section; Haversian porosity (HP) and ultrastructure (US) correspond to black and gray regions, respectively. (b) Typical RVE, *i.e.* cubic region with edge length of 50 voxels $\sim$ 0.5 mm; GLs are represented using the "jet" color-map of Matlab. (c) GL distribution in the RVE and threshold q between HP and US. (d) TMD distribution in the US and average value $\overline{\mathrm{TMD}}$. (For interpretation of the references to color in this figure legend, the reader is referred to the Web version of this article.)

a cubic region with edge length = 50 voxels ∼ 0.5 mm). On the other side, TMD is defined at the US scale and was measured on a voxel-wise basis (see inset (d) in Fig. 2, voxel size = $10.13 \, \mu m$). Moreover, starting from the TMD distributions of each RVE, tissue-scale average values of TMD, denoted $\overline{\text{TMD}}$, can be computed. Therefore, the pair ($\overline{\text{TMD}}$, HP) collects experimental measures referring at the tissue scale.

2.3. Experimental data from $\text{SR} - \mu\text{CT}$ imaging

Experimental data are collected using the protocol described in our previous studies (Sansalone et al., 2016). For sake of completeness, the main steps are reported here below.

A bone sample, extracted from the inferior femoral neck of a 79-year-old patient undergoing standard hemiarthroplasty, has been imaged using synchrotron radiation micro-computed tomography ($\text{SR} - \mu\text{CT}$) at the European Synchrotron Radiation Facility (ESRF, Grenoble, France). Image reconstruction was performed in a *volume of interest* (VoI) of $660 \times 660 \times 523$ isotropic voxels (size $10.13 \, \mu m$). The outcome was a 3-D GL mapping (GL range: [0,255]) of the linear attenuation coefficient of the monochromatic X-ray beam. Regions corresponding to Haversian pores (HP) and ultrastructure (US) were identified by fixing a lower threshold $q = 131$ for US voxels (see Sec. 2.2 for more details).

After segmentation of the bone sample with Simpleware ScanIP software (Simpleware 5.0 ScanIP+, 2012), 35 representative volume elements (RVEs) were selected in the cortical part of the VoI spanning the sample in the axial and hoop direction. Following Sansalone et al. (2016), RVEs were taken as cubic regions with edge length of $N_{\text{vox}} = 50$ voxels, *i.e.* about $0.5 \, mm$. The relevant RVEs were extracted from the bone sample at about $1.5 \, mm$ from the periosteum (distance measured with respect to the center of the RVEs) and at different hoop and axial positions with respect to a cylindrical frame centred at the anatomical axis of the bone sample, avoiding volume overlapping. The global reference frame on the bone sample, the local reference frame on a RVE and the location of the RVEs are presented in Fig. 3. For the global reference, the unit vector e_3 is aligned with the axis of the femoral neck and the unit vectors e_1 and e_2 lie in the plane of the cross section of the sample. For the local reference, the first axis e_t is aligned to the tangential direction formed by the circumferential line (see Fig. 3), the second axis e_r is oppositely aligned to the radial vector of the sample and the third axis e_z is aligned to e_3 of the global reference. The origin of the local frame is placed at the center of the RVE. Coordinates x_3 and θ refer to the axial and hoop coordinates of the centers of the RVEs, respectively. The axial coordinate x_3 is the distance of the center of the RVE from the distal part of the sample (). The hoop coordinate θ is the

angle measured counterclockwise with respect to the inferior axis of the sample ($\theta = 0$). The complete dataset, statistically representing the whole VoI, has been divided in two parts. A calibration subset (*Calib* dataset, red RVEs in Fig. 3) consisting of 12 RVEs, has been used to obtain input data (statistics of HP and $\overline{\text{TMD}}$) for the stochastic and nominal models (see Sec. 2.4). The remaining 23 RVEs have been used for validation purposes (*Ctrl* dataset, light red RVEs in Fig. 3). The complete dataset has been used to build microstructural μFE and μFFT models.

2.4. Statistical information on HP and $\overline{\text{TMD}}$ from $\text{SR} - \mu\text{CT}$ images

Information on the composition of the cortical tissue was obtained by analyzing the *Calib* dataset of RVEs. This dataset constitutes a systematic sampling of the overall population of cortical RVEs and was used to estimate the statistics (namely, mean value and dispersion) of HP and $\overline{\text{TMD}}$ in the cortical tissue. A database consisting of RVE-wise pairs ($\overline{\text{TMD}}$, HP) was constituted. Within each RVE, the HP and the voxel-wise distribution of TMD were computed by means of Eqs. (2.1)–(2.3). Then, the voxel-wise distribution of TMD was averaged to compute $\overline{\text{TMD}}$.

Statistics (namely, mean value, standard deviation, and dispersion) of the database of ($\overline{\text{TMD}}$, HP) RVE-wise values were computed and assumed to be representative of the tissue-scale composition of the whole cortical tissue. In the framework of a *parametric probabilistic* approach, the uncertainty on a measured variable x is taken into account by replacing x by a real-valued random variable X. Hereafter, capital letters will refer to random variables. Let X be either of HP or $\overline{\text{TMD}}$, and let $\mu_X^{\exp}$, $\sigma_X^{\exp}$ and $\delta_X^{\exp}$ be the set of *known parameters* (the mean value, standard deviation, and dispersion of X, respectively). Their values were estimated through the respective stochastic estimators $\hat{\mu}_X^N$, $\hat{\sigma}_X^N$ and $\hat{\delta}_X^N$, reading:

$$\hat{\mu}_X^N = \frac{1}{N} \sum_{k=1}^{N} x_k,$$
$$\hat{\sigma}_X^N = \left[\frac{1}{N-1} \sum_{k=1}^{N} (x_k - \hat{\mu}_X^N)^2 \right]^{\frac{1}{2}},$$
$$\hat{\delta}_X^N = \frac{\hat{\sigma}_X^N}{\hat{\mu}_X^N}, \tag{2.4}$$

where x_i is the i-th experimental measure of X and N is the number of measures. As long as measures x_i are statistically representative of the whole cortical tissue, descriptive statistics in Eq. (2.4) provide an accurate estimate of the overall experimental statistics:

$$\mu_X^{\exp} \sim \hat{\mu}_X^N, \quad \sigma_X^{\exp} \sim \hat{\sigma}_X^N, \quad \text{and} \quad \delta_X^{\exp} \sim \hat{\delta}_X^N. \tag{2.5}$$
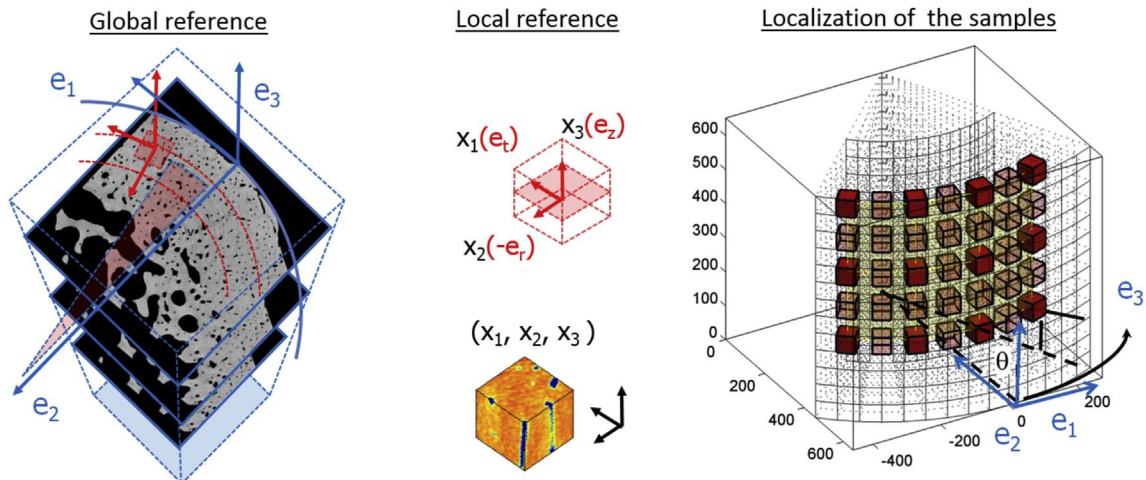

Fig. 3. Global and local reference frames on the bone sample and on a typical RVE, respectively, and localization of the RVEs (red and light red cubes refer to *Calib* and *Ctrl* datasets, respectively). See text for more details. (For interpretation of the references to color in this figure legend, the reader is referred to the Web version of this article.)
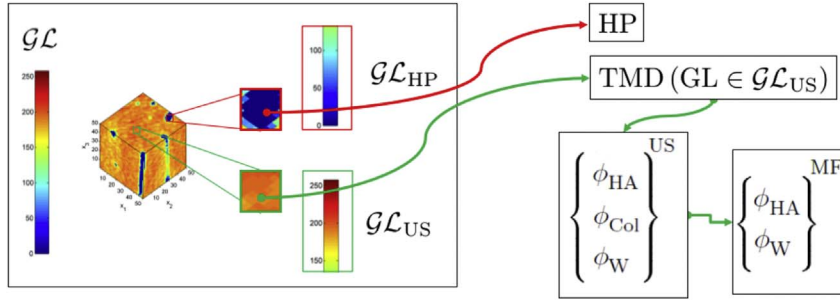
Fig. 4. Sketch of the procedure for evaluating the HP, $\overline{TMD}$, and VFs in a RVE.

Table 1
Elastic properties of essential constituents of bone.

water	(MF)	$K = 2.3\,[GPa]$	$G = 0\,[Pa]$
	(HP/μ-mech. & FFT)	$K = 2.3\,[GPa]$	$G = 0\,[Pa]$
	(HP/FEM)	$K = 2.3\,[GPa]$	$G = 1\,[MPa]$
HA		$Y = 120\,[GPa]$	$\nu = 0.27 \quad [-]$
Collagen		$c_{1111} = 11.7\,[GPa]$	
		$c_{3333} = 17.9\,[GPa]$	
		$c_{1122} = 5.1\,[GPa]$	
		$c_{1133} = 7.1\,[GPa]$	
		$c_{1313} = 3.3\,[GPa]$	

2.5. Volume fractions of essential constituents

The measures of HP and $\overline{TMD}$ have been used to compute the (average) volume fractions (VFs) of each phase at each level of the hierarchical description of bone introduced in Sec. 2.1. The procedure is summarized below for sake of completeness and Fig. 4 shows a sketch of the procedure for evaluating the HP, $\overline{TMD}$, and VFs in a RVE.

CB-scale. Within each RVE of cortical bone (CB), the VF of HP (denoted by ϕ_{HP}^{CB}) was computed as the relative number of voxels with GL $\in \mathscr{GL}_{HP}$ (see Eq. (2.3)). Then, the VF of the ultrastructure (US) turns out to be: $\phi_{US}^{CB} = 1 - \phi_{HP}^{CB}$.

US-scale. VFs of hydroxyapatite (HA), collagen (Col), and water (W) in the ultrastructure (US) ϕ_{HA}^{US}, ϕ_{Col}^{US}, and ϕ_{W}^{US}, respectively–were computed from $\overline{TMD}$ by solving the nonlinear system (Broz et al., 1995):

$$\begin{cases} \phi_{HA}^{US} = \dfrac{\overline{TMD}}{\rho_{HA}}, \\ \phi_{HA}^{US} + \phi_{Col}^{US} + \phi_{W}^{US} = 1, \\ \dfrac{\phi_{Col}^{US}}{\phi_{W}^{US}} = \alpha + \beta \times \exp(\gamma \times \phi_{HA}^{US}), \end{cases} \quad (2.6)$$

where $\alpha = 0.36$, $\beta = 0.084$ and $\gamma = 6.7$. First, ϕ_{HA}^{US} was directly computed by dividing $\overline{TMD}$ by the mass density of the mineral ($\rho_{HA} = 3\,g/cm^3$) (see Eq. (2.6)/1). Then, ϕ_{Col}^{US} and ϕ_{W}^{US} are computed by supplementing the volume balance equation (see Eq. (2.6)/2) with an empirical relation (see Eq. (2.6)/3).

MF-scale. VFs of mineral and water in the mineral foam (MF) have been evaluated from their counterparts at the US scale by simply preserving their relative amount after downscaling:

$$\begin{cases} \phi_{HA}^{MF} = \dfrac{\phi_{HA}^{US}}{(\phi_{HA}^{US} + \phi_{W}^{US})}, \\ \phi_{W}^{MF} = \dfrac{\phi_{W}^{US}}{(\phi_{HA}^{US} + \phi_{W}^{US})}. \end{cases} \quad (2.7)$$

Bone composition at the US and MF scales is fully described by ϕ_{Col}^{US} and ϕ_{HA}^{MF}, respectively. These VFs are both computed from $\overline{TMD}$ by solving Eqs. (2.6) and (2.7) which can be restated implicitly as:

$$\phi_{Col}^{US} = \hat{\phi}_{Col}^{US}(\overline{TMD}), \qquad \phi_{HA}^{MF} = \hat{\phi}_{HA}^{MF}(\overline{TMD}). \quad (2.8)$$

Equation (2.6)/3 was obtained by Raum et al. (2006) based on experimental data of Broz et al. (1995). The formula fits the experimental data with a coefficient of adjusted determination $R^2 = 0.996$ (see Raum et al. (2006)) proving its effectiveness in describing the relative amount of US constituents. Equation (2.7) just state that the mineral foam (subscript MF) is composed only of mineral (subscript HA) and absorbed water (subscript w). Equation (2.8) follow from Eqs. (2.6) and (2.7).

2.6. Elastic properties of essential constituents

The models presented in this work are described as mixtures of three essential constituents which are mineral (hydroxyapatite), water and collagen. Elastic properties of these three constituents are supposed to be known and their values were adapted from Hellmich et al. (2004a) and reported in Table 1. Specifically, the mineral and the water have been assumed as *isotropic* materials (with bulk *modulus K*, shear *modulus G*, Young's *modulus Y* and Poisson's ratio ν). Water has been assumed as a compressible fluid with zero shear *modulus*. (In the FEM models of cortical bone, in order to avoid numerical problems, the shear *modulus* of water filling the Haversian pores was assumed much smaller than its bulk *modulus*.) Collagen has been assumed as a *transversely isotropic* material with the axis of symmetry aligned with the pore direction (see the $\mathbf{e}_3$-direction in Fig. 3).

2.7. Stochastic micromechanical (SμM) model of cortical bone

The variability of the elastic properties of the cortical bone at the tissue scale can be described by introducing a suitable stochastic model of the input data ($\overline{TMD}$,HP) in the micromechanical model described in Sec. A.1. Hereinafter, this will be referred to as a stochastic micromechanical (SμM) model of cortical bone. Probabilistic model should be such that the statistics of the random variables $\overline{TMD}$ and HP correspond to the statistics obtained from the available information *via* the experimental data of the TMD and HP.

2.7.1. Stochastic models of $\overline{TMD}$ and HP

Scattering of the experimental measures of $\overline{TMD}$ and HP in the region of interest are represented in Fig. 5. Analysis of the *Calib* dataset (solid circles in Fig. 5) shows a low correlation between $\overline{TMD}$ and HP with a correlation coefficient $r(\overline{TMD},HP) = 0.0915$.

Uncertainties on the actual values of $\overline{TMD}$ and HP were accounted for by modeling them as random variables. Let $\mathbf{X} := (X_1, X_2)$ be the random vector modeling the pair ($\overline{TMD}$,HP). In view of the very small correlation between $\overline{TMD}$ and HP, X_1 and X_2 can be modeled as statistically independent random variables. Then, the probability density function (PDF) of $\mathbf{X}$, denoted by $p_{\mathbf{X}}(\mathbf{x})$, reads:

$$p_{\mathbf{X}}(\mathbf{x}) \equiv p_{X_1}(x_1) \times p_{X_2}(x_2), \quad (2.9)$$

where $p_{X_1}(x_1)$ and $p_{X_2}(x_2)$ are PDFs of X_1 and X_2 respectively.

The expression of each $p_{X_i}(x_i)$ (with $i = 1,2$) was obtained by means of the Maximum-Entropy (denoted by MaxEnt) principle. The MaxEnt principle (Jaynes, 1957a, b; Soize, 2001) allows building the PDF $p_X(x)$

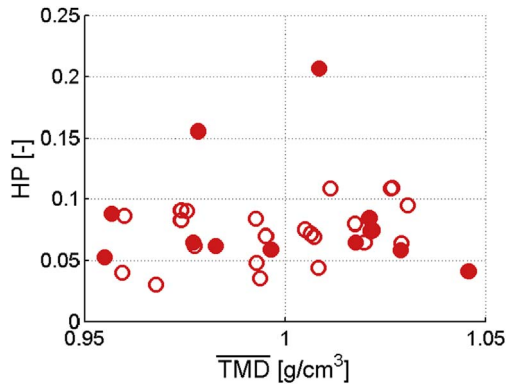**Fig. 5.** Scatter plot of the pairs of measures ($\overline{\text{TMD}}$,HP) for each of RVE$_i$ related to the *Calib* (solid circles) and *Ctrl* (empty circles) datasets.

of a random variable X by maximizing the *measure of uncertainty* given by the Shannon's entropy (Shannon, 1948) under a given set of constraints. These latter can be stated in terms of preservation of some statistics of X which are assumed to represent the only *available information*. The general form of the Shannon's entropy for the random variable X reads:

$$\mathscr{S}(p_X) = \int_{S_X} -\ln(p_X(x))\, p_X(x)\, dx \tag{2.10}$$

where ln designates the natural logarithm function and S_X the support of the random variable X. In the context of this paper, available information on X was assumed to be given in terms of its support S_X, mean value μ_X and standard deviation σ_X–or, equivalently, dispersion $\delta_X = \sigma_X/\mu_X$. The constraints are specified by taking:

$$
\begin{aligned}
\mathbb{E}(\mathbb{1}_{S_X}(X)) &= 1\,; \\
\mathbb{E}(X) &= \mu_X^{\exp}\,; \\
\mathbb{E}(X^2) &= (\mu_X^{\exp})^2 \times (1 + (\delta_X^{\exp})^2)\,.
\end{aligned}
\tag{2.11}
$$

where

$$\mathbb{E}(f(X)) = \int_{\mathbb{R}} f(x) \times p_X(x)\, dx\,, \tag{2.12}$$

where $\mathbb{E}(*)$ designates the mathematical expectation and $\mathbb{R}$ is the real axis.

In Eq. (2.11), $\mathbb{1}_{S_X}(x)$ is the characteristic function of S_X, $\mu_X^{\exp}$ and $\delta_X^{\exp}$ are experimental statistics. The constraint given by (2.11)/1 is the normalization condition on the PDF of X. Constraints given by (2.11)/2 and (2.11)/3 fix the values of the two first moments of X through the available *experimental information*. This is equivalent to enforce the mean value and dispersion of X to be equal to their corresponding experimental values, *i.e.* $\mu_X = \mu_X^{\exp}$ and $\delta_X = \delta_X^{\exp}$. In particular, the support of X_1 is formed by the set to the points obtained through Eq. (2.1), *i.e.* $S_{X_1} = [0.7; 1.5]$; and the support of X_2 has been set to $S_{X_2} = [0,1]$.

The solution of the above constrained maximization problem leads to the PDF of X, reading (Soize, 2004; Sansalone et al., 2016):

$$p_X^{\lambda^*}(x) := \mathbb{1}_{S_X}(x)\exp\{-(\lambda_0^* + \lambda_1^* x + \lambda_2^* x^2)\}, \tag{2.13}$$

where the vector $\lambda^* := [\lambda_0^*, \lambda_1^*, \lambda_2^*]$ is an hyperparameter of the PDF which should be determined by maximining the functional given by Eq. (2.10) under the constraints given by Eq. (2.11). The integrability conditions impose the following relations on the components of the hyperparameter λ:

$$\lambda_0 \in \mathbb{R}, \quad \lambda_1 < 0, \quad \lambda_2 > 0. \tag{2.14}$$

Note that the PDF coming from this specific problem corresponds to the truncation of the PDF of the Gaussian random variable $\mathscr{G}(\mu_g, \sigma_g)$ (with $\sigma_g = 1/(2\lambda_2)$, $\mu_g = -\lambda_1 \times \sigma_g$) on the support S_X.

2.7.2. Numerical solution of the stochastic models of $\overline{\text{TMD}}$ and HP

In order to obtain the realizations of both random variables, we proceed in two steps.

Step 1/Definition of the PDF of $\overline{\text{TMD}}$ and HP.

Firstly, the PDFs of $\overline{\text{TMD}}$ and HP have been computed. This step implies the research of the optimal vector λ^*. This operation has been accomplished using the simplex method (Ciarlet, 1989).

The convergence rate of any iterative optimization method depends on the choice of the first guess $\lambda^{(0)} = [\lambda_0^{(0)}, \lambda_1^{(0)}, \lambda_2^{(0)}]$. Setting a "good" initial guess should be performed using some *heuristic*. It is possible to show that for a PDF like that defined by Eq. (2.13), the proximity of the mode estimation to the mean value of X leads to the following choice of the guess:

$$
\begin{cases}
\lambda_1^{(0)} := a \times \lambda_2^{(0)}, \quad \text{where } a = -2\mu_X, \\
\lambda_0^{(0)} = \ln\left(\int_{S_X} \exp-(\lambda_1^{(0)}x + \lambda_2^{(0)}x^2)\, dx\right).
\end{cases}
\tag{2.15}
$$

Moreover, increasing the value of $\lambda_2^{(0)}$ induces a reduction of the dispersion δ_X.

Step 2/Collection of statistically independent realizations of $\overline{\text{TMD}}$ and HP

A set of statistically independent realizations of $\overline{\text{TMD}}$ and HP were computed using the *pseudo-inverse* method (Devroye, 1986). Let X be any of X_1 or X_2 and $F_X^{\lambda^*}(x)$ its repartition function given by:

$$F_X^{\lambda^*}(x) = \int_{-\infty}^x p_X^{\lambda^*}(y)\, dy. \tag{2.16}$$

Firstly, the *pseudo-inverse* $\left(F_X^{\lambda^*}\right)^{-1}$ of the repartition function was numerically computed. Then, a large number N of realizations of a *uniform* random variable U with values in $[0, 1]$ were collected. Eventually, for each realization $U(a_i)$ for $i = 1, ..., N$, a realization of X was computed as:

$$X(a_i) = \left(F_X^{\lambda^*}\right)^{-1}(U(a_i))\,. \tag{2.17}$$

2.7.3. Stochastic micromechanical model of cortical bone elasticity

Stochastic model of uncertainties of cortical bone (CB) composition can be obtained by means of the realizations $X_1(a_i)$ and $X_2(a_i)$ (with $i = 1, ..., N$) of the random variables modeling the uncertains $\overline{\text{TMD}}$ and HP, respectively.

In a first step, realizations of the random elasticity tensors of the mineral foam (MF) and ultrastructure (US) were computed using the procedure described in the follow. Roughly, the realizations $X_1(a_i)$ (random $\overline{\text{TMD}}$) were used to compute the corresponding values of random VFs at the US and MF scales through Eqs. (2.6)–(2.7) (hereinafter, capital letters will denote random VFs):

$$
\begin{cases}
\Phi_{\text{HA}}^{\text{US}}(a_i) = \hat{\phi}_{\text{HA}}^{\text{US}}(X_1(a_i)), \quad \Phi_{\text{Col}}^{\text{US}}(a_i) = \hat{\phi}_{\text{Col}}^{\text{US}}(X_1(a_i)), \\
\Phi_{\text{W}}^{\text{US}}(a_i) = \hat{\phi}_{\text{W}}^{\text{US}}(X_1(a_i)), \\
\Phi_{\text{HA}}^{\text{MF}}(a_i) = \hat{\phi}_{\text{HA}}^{\text{MF}}(X_1(a_i)), \quad \Phi_{\text{W}}^{\text{MF}}(a_i) = \hat{\phi}_{\text{W}}^{\text{MF}}(X_1(a_i)).
\end{cases}
\tag{2.18}
$$

In turn, these values of random VFs were used to compute the realizations of the random elasticity tensors of the MF and US through Eqs. (A.9) and (A.10), respectively. Using the synthetic form of Eq. (A.11), these equations read:

$$
\begin{aligned}
g_I^{\text{SC}}(\mathbb{C}_{\text{MF}}(a_i); \Phi_{\text{HA}}^{\text{MF}}(a_i), \{\mathfrak{c}_{\text{HA}}, \mathfrak{c}_{\text{W}}\}) = 0 \quad \text{leads to } \mathbb{C}_{\text{MF}}(a_i)\,, \\
g_{II}^{\text{MT}}(\mathbb{C}_{\text{US}}(a_i); \Phi_{\text{Col}}^{\text{US}}(a_i), \{\mathfrak{c}_{\text{HA}}, \mathfrak{c}_{\text{W}}(a_i)\}) = 0 \quad \text{leads to } \mathbb{C}_{\text{US}}(a_i)\,.
\end{aligned}
\tag{2.19}
$$

In a second step, realizations of the random elasticity tensor of CB were computed by using the realizations $X_2(a_i)$ (random HP) and $\mathbb{C}_{\text{US}}(a_i)$ as input data of Eq. (A.10). Using the synthetic form of Eq. (A.11), this equation reads:

$$g_{III}^{\text{MT}}(\mathbb{C}_{\text{CB}}(a_i); X_2(a_i), \{\mathfrak{c}_{\text{W}}, \mathbb{C}_{\text{US}}(a_i)\}) = 0 \quad \text{leads to } \mathbb{C}_{\text{CB}}(a_i)\,. \tag{2.20}$$

We observe here that all the realizations of the stochastic tensors stay in the same symmetry group of their deterministic counterparts; that is $\mathbb{C}_{MF}(a_i)$ is isotropic whereas $\mathbb{C}_{US}(a_i)$ and $\mathbb{C}_{CB}(a_i)$ are transversely isotropic. Moreover, thanks to the *closure property* of the *elastic symmetry groups*, also the mean values of these stochastic tensors stay in the same symmetry classes (see Appendix C).

2.7.4. Statistical analysis of random elastic coefficients

An overall picture of the elasticity of bone at all scales (mineral foam, ultrastructure and cortical tissue) can be given in terms of statistics of individual *moduli* or whole tensors. On the one side, statistics (mean value, dispersion and confidence intervals) of elastic *moduli* were estimated by means of the stochastic estimators in Eq. (2.4). On the other side, mean value and dispersion of a random tensor $\mathbb{C}$ (named $\mu_{[\mathbb{C}]}$ and $\delta_{[\mathbb{C}]}$, respectively, by making use of Kelvin representation for $[\mathbb{C}]$) were estimated through the statistical estimators:

$$\mu_{[\mathbb{C}]}^N = \frac{1}{N} \sum_{k=1}^{N} [\mathbb{C}(a_k)],$$

$$\delta_{[\mathbb{C}]}^N = \sqrt{\frac{\frac{1}{N} \sum_{k=1}^{N} \left\| [\mathbb{C}(a_k)] - \mu_{[\mathbb{C}]}^N \right\|_F^2}{\left\| \mu_{[\mathbb{C}]}^N \right\|_F^2}} \, , \tag{2.21}$$

where $\|\cdot\|_F$ is the Frobenius' norm of a square matrix. The dispersion $\delta_{[\mathbb{C}]}$ represents a global measure of the fluctuations of $[\mathbb{C}]$ around its mean value $\mu_{[\mathbb{C}]}$.

2.8. Nominal micromechanical (NμM) model of cortical bone

A nominal micromechanical (NμM) model of cortical bone was developed corresponding to the mean model of the stochastic micromechanical SμM model. First, RVE-wise values of $\overline{TMD}$ and HP were averaged on the *Calib* dataset ($\mu(\overline{TMD}) = \mu_{TMD}^{exp}$, $\mu(HP) = \mu_{HP}^{exp}$) and used to obtain average values of the VFs of bone constituents by means of the relations introduced in Sec. 2.5:

$$\mu_{HP}^{exp} \rightarrow \phi_{HP}^{CB} = \hat{\phi}_{HP}^{CB}(\mu_{HP}^{exp}),$$

$$\mu_{TMD}^{exp} \rightarrow \begin{cases} \phi_{HA}^{US} = \hat{\phi}_{HA}^{US}(\mu_{TMD}^{exp}), & \phi_{Col}^{US} = \hat{\phi}_{Col}^{US}(\mu_{TMD}^{exp}), \\ \phi_{W}^{US} = \hat{\phi}_{W}^{US}(\mu_{TMD}^{exp}), \\ \phi_{HA}^{MF} = \hat{\phi}_{HA}^{MF}(\mu_{TMD}^{exp}), & \phi_{W}^{MF} = \hat{\phi}_{W}^{MF}(\mu_{TMD}^{exp}). \end{cases} \tag{2.22}$$

Then, these average VFs were used to compute the nominal elasticity tensors of MF, US and CB by means of Eq. (A.11), reading:

$$g_I^{SC}(\mathbb{c}_{MF}; \phi_{HA}^{MF}, \{\mathbb{c}_{HA}, \mathbb{c}_W\}) = 0 \text{ leads to } \mathbb{c}_{MF},$$

$$g_{II}^{MT}(\mathbb{c}_{US}; \phi_{Col}^{US}, \{\mathbb{c}_{HA}, \mathbb{c}_{MF}\}) = 0 \text{ leads to } \mathbb{c}_{US},$$

$$g_{III}^{MT}(\mathbb{c}_{CB}; \phi_{HP}^{CB}, \{\mathbb{c}_W, \mathbb{c}_{US}\}) = 0 \text{ leads to } \mathbb{c}_{CB}. \tag{2.23}$$

2.9. Micro-finite element (μFE) model of cortical bone

Finite element (FE, see Sec. A.2) models of bone microstructure, referred to as μFE models, were used to compute the effective elastic properties of all the RVEs (*Calib* and *Ctrl* datasets) represented in Fig. 3. These models accounted for the actual morphology of the RVEs and a simplified representation of their heterogeneous elastic properties.

The numerical procedure, shortly reported in (Sansalone et al., 2016), is outlined here below. Starting from a structured isotropic regular mesh (50^3 cubic voxels points) of the RVE, a coarser tetrahedral mesh was generated using Simpleware software (Simpleware 5.0 ScanIP+, 2012) for reducing the computational cost. The region corresponding to the US (voxels with GL in $\mathscr{GL}_{US}$) was divided in n_{ph} subregions by dividing the whole set of GL-range $\mathscr{GL}_{US}$ in n_{ph} equal subsets $\mathscr{GL}_{US}^{(n)}$, with $n = 1, ..., n_{ph}$. Grey levels in each subregion were further replaced by their mean value. The region corresponding to the

HP and the subregions corresponding to the US were meshed by preserving mesh coherence between adjacent regions. The mesh and the GLs associated to each subregion were exported to COMSOL Multiphysics software (COMSOL Multiphysics, 2015). COMSOL Multiphysics was used with second-order Lagrangian finite elements based on the geometric mesh exported by Simpleware. Elastic properties of the FE were assigned based on their GLs. Material properties of finite elements belonging to the HP region were given by the elastic properties of water resumed in Table 1. Continuum micromechanics was used to compute the elastic properties of the FEs belonging to US regions. Specifically, the GL of each US region was converted in TMD (see Eq. (2.1)) and then in VFs of bone constituents at the MF and US scales (Eq. (2.6)–(2.7)) which, in turn, were used to compute the elasticity tensors of the MF and US (Eq. (2.23), steps *I* and *II*).

The number n_{ph} of US subregions was defined by performing a preliminary parametric study and looking for stabilization of FE results with respect to n_{ph}. Results obtained for 8 and 16 subregions being quite similar, the value $n_{ph} = 8$ was used hereinafter.

2.10. Micro-Fast Fourier Transform (μFFT) model of cortical bone

Models of bone microstructure based on the Fast Fourier Transform (FFT, see Sec. A.3), referred to as μFFT models, were used to compute the effective elastic properties of all the RVEs (*Calib* and *Ctrl* datasets) represented in Fig. 3. These models accounted for the actual morphology and heterogeneous distribution of elastic properties of the RVEs.

Calculations were performed by using the *CraFT* software (Composite response and Fourier Transforms) (Moulinec and Suquet, 1998). Each RVE was represented as a vector collecting the GLs of all the $N = N_1 \times N_2 \times N_3 = 50^3 = 125000$ voxels of the RVE. A threshold $q = 131$ was used to separate the voxels belonging to the US from those belonging to the HP. Elastic properties of water (see Table 1) were given to the voxels belonging to the HP. The material properties associated with the voxels belonging to the US were computed applying the fist two step of the continuum micromechanics model to those volume fractions corresponding to the specific grey level. Specifically, the GL of each voxel was converted in TMD (see Eq. (2.1)) and then in VFs of bone constituents at the MF and US scales (see Eqs. (2.6)–(2.7)) which, in turn, were used to compute the elasticity tensors of the MF and US (see Eq. (2.23), steps *I* and *II*).

The determination of the effective macroscopic elastic properties of any RVE is accomplished if the 36 components c_{ij} of any representation of the elasticity tensor $\mathbb{c}^*$ are defined. We have estimated $\mathbb{c}^*$ column by column evaluating 6 stress vectors $\mathbf{S}^*$ results corresponding to 6 linearly independent strain assignments $\mathbf{E}^*$ according to the algorithm described in sec. A.3. The calculation have been run until the error from equilibrium condition (see Eq. (A.22)) reduced to $< 10^{-4}$.

The six strain tests $\mathbf{E}^*$ are expressed in the Kelvin representation:

$$[\mathbf{E}^*] = [\mathbf{E}^*]_1, [\mathbf{E}^*]_2, [\mathbf{E}^*]_3, [\mathbf{E}^*]_4, [\mathbf{E}^*]_5, [\mathbf{E}^*]_6$$

$$= \begin{bmatrix} 1 \\ 0 \\ 0 \\ 0 \\ 0 \\ 0 \end{bmatrix}, \begin{bmatrix} 0 \\ 1 \\ 0 \\ 0 \\ 0 \\ 0 \end{bmatrix}, \begin{bmatrix} 0 \\ 0 \\ 1 \\ 0 \\ 0 \\ 0 \end{bmatrix}, \begin{bmatrix} 0 \\ 0 \\ 0 \\ 1 \\ 0 \\ 0 \end{bmatrix}, \begin{bmatrix} 0 \\ 0 \\ 0 \\ 0 \\ 1 \\ 0 \end{bmatrix}, \begin{bmatrix} 0 \\ 0 \\ 0 \\ 0 \\ 0 \\ 1 \end{bmatrix}, \tag{2.24}$$

where $[\mathbf{E}^*]_i$ for $i = 1, ..., 6$ designates the test given homogeneous strain.

3. Results and discussion

The presentation of the results is organized as follows: first, the numerical set up of the stochastic models of $\overline{TMD}$ and HP is described; second, results of the stochastic micromechanical (SμM) model of cortical bone are shown and compared with those of the nominal micromechanical (NμM) model; then, the results of the microstructural μFE

Table 2
Experimental statistics of the *Calib* dataset.

HP [−]		$\overline{\text{TMD}}$ [g/cm³]	
μ^{exp}	δ^{exp}	μ^{exp}	δ^{exp}
0.084	0.547	0.999	0.028

and μFFT models are presented; eventually, the SμM model is validated against the μFE and μFFT models and its accuracy assessed. Remarks about the propagation of uncertainty through the scales and the impact of the range of gray scale values conclude this section.

3.1. Numerical set up of the stochastic models of $\overline{\text{TMD}}$ and HP

Experimental statistics of $\overline{\text{TMD}}$ and HP (estimated through Eqs. (2.4)–(2.5)) are reported in Table 2. Data refer to the *Calib* dataset. The average value of HP is 8.4%–a normal result in healthy subjects whose typical HP is in the range [5 %− 10%]. Since the mineralization can vary significantly from one anatomical site to another (we have observed values of TMD of about $1.2\,g/cm^3$ in μCT images of human fibula, data not shown), the value of average mineralization of about $1\,g/cm^3$ is to be considered site- and patient-specific. It is worth noting that the dispersion of $\overline{\text{TMD}}$ is very low (<0.05), while that of HP is quite high (>0.5).

Data in Table 2 have been considered as the available information about $\overline{\text{TMD}}$ and HP and used to obtain the PDFs of the associated random variables. The components of optimal vector defined in the PDFs of Eq. (2.13) are given by:

$$\lambda^*_{\overline{\text{TMD}}} = [580.86, \ -1167.89, \ 584.42],$$
$$\lambda^*_{\text{HP}} = [-1.23, \ -22.45, \ 153.22]. \tag{3.1}$$

Convergence of the statistical estimators of the mean value and dispersion of the stochastic models of $\overline{\text{TMD}}$ and HP towards the experimental values has been tested looking at the absolute and relative errors defined by:

$$\Delta^N(\cdot)_X = \left[\widehat{(\cdot)}^N_X - (\cdot)^{exp}_X\right], \quad \Delta^N_{rel}(\cdot)_X = \frac{\Delta^N(\cdot)_X}{(\cdot)^{exp}_X}, \tag{3.2}$$

where $(\cdot)_X$ is a statistic of X. Convergence plots of the relative errors of the mean values and of the absolute errors of the dispersions are shown in Fig. 6. Convergence is assumed to be reached after $N = 10^5$ realizations when all the errors are smaller than 10^{-3}. This result was further validated looking at the convergence of the statistical estimators of the statistics of the elastic *moduli* of CB (see Fig. 7). In Fig. 7, the confidence interval (denoted by CI) is shown. Therefore, hereinafter, statistics of the stochastic models will refer to $N = 10^5$ realizations.

3.2. Stochastic and nominal micromechanical models of cortical bone elasticity

Statistics of the random elastic *moduli* (SμM model, $N = 10^5$

realizations) and corresponding nominal values (NμM model) are reported in Table 3. The relative differences between the stochastic estimators of the mean values and the nominal values of all the elastic *moduli* are smaller than 1% (and even smaller than 0.1% for the ratio ν_{31}). This shows that the nominal model constitutes an accurate description of the mean elastic behavior of the cortical bone.

An analysis of the Table 3 shows that the mean values of all the random *moduli* (except for ν_{13}) overestimate the corresponding nominal *moduli*. This can be explained by a qualitative analysis and making use of the *Jensen's inequality* reported in Appendix D (see Fig. 12 and comments about these figures in section 3.6). In particular, these figures (see Fig. 12) show that the surfaces representing the elastic *moduli* as a function of the model random variables ($\overline{\text{TMD}}$,HP) are convex (except for ν_{13}, which is concave) in the 99% *confidence region* of the space ($\overline{\text{TMD}}\times$HP) (*i.e.* the region of the space ($\overline{\text{TMD}}\times$HP) containing 99% of the realizations of the elastic *moduli*). Therefore, by making use of the Jensen's inequality, it is possible to conclude that the nominal value of each elastic *modulus* (except for ν_{13}) underestimates the mean value of the realizations of its stochastic counterpart. Note that this result will hold true yet by changing the stochastic models of $\overline{\text{TMD}}$ and HP as long as the 99% *confidence region* does not change noticeably.

Mean values and dispersions (see Eq. (2.21)) of the elasticity tensors $[\mathbb{C}_*]$, in which the subscript * designates MF, US and CB, are reported in Tables 4 and 5, respectively. These two pieces of information ($\hat{\mu}^N_{[\mathbb{C}_*]}$ and $\hat{\delta}^N_{[\mathbb{C}_*]}$) constitute the minimal necessary parameters for defining elasticity tensors in the same symmetry class (see Guilleminot and Soize (2013)) and could be useful in further works.

The elasticity tensors of MF, US and CB can be represented as linear combinations of the base tensors of their respective symmetry classes (see Appendix C). The mean values of the base coefficients (*i.e.* the coefficients of the linear combinations) predicted by the SμM model are reported in Table 4.

The dispersions of the elasticity tensors of MF, US and CB are reported in Table 5. It can be noted that the dispersion decreases when upscaling from the MF scale to the US scale– because of the weak dispersion of collagen then increases again when upscaling to the CB scale– because of the large dispersion of HP (see Table 2).

3.3. Results of the μFE and μFFT models

The FEM and FFT methods have been applied to all the RVEs (35 RVEs overall, 12 in the *Calib* dataset and 23 in the *Ctrl* dataset).

Both models produce anisotropic effective elastic tensors for the CB. Let $\mathbb{c}$ be an anisotropic elasticity tensor. It was projected onto the classes of transversely isotropic and orthotropic tensors to investigate to what extent CB can be considered as a transversely isotropic material. In what follows, the transversely isotropic and orthotropic symmetry classes are denoted by TI for which the transverse axis is $\mathbf{e}_3$-direction and O respectively. Let $[\mathbb{c}]$ be the Kelvin's matrix representation of the elastic fourth-order tensor $\mathbb{c}$, let $\mathscr{P}_S([\mathbb{c}])$ with $S \in \{\text{TI, O}\}$ (see Appendix C) to be the projected matrix on the class of material symmetry S and, $E_S([\mathbb{c}])$ the distance of $[\mathbb{c}]$ from $\mathscr{P}_S([\mathbb{c}])$:
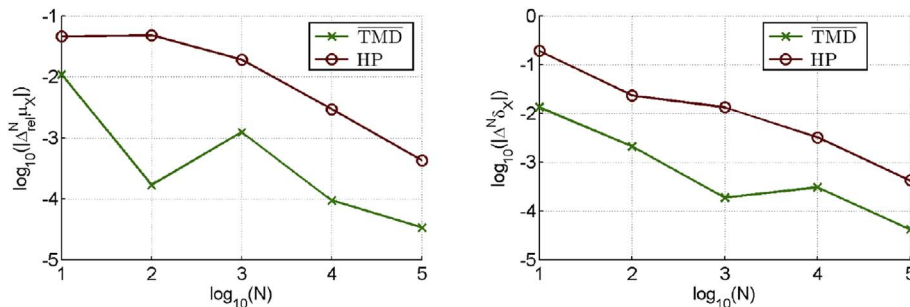
Fig. 6. Convergence plots of the stochastic models of $\overline{\text{TMD}}$ (green lines with 'x' markers) and HP (dark red lines with 'o' markers): relative error of the mean values (on the left) and absolute error of the dispersions (on the right) as a function of the number of realizations. $\log_{10}$ is the base 10 logarithm function. (For interpretation of the references to color in this figure legend, the reader is referred to the Web version of this article.)
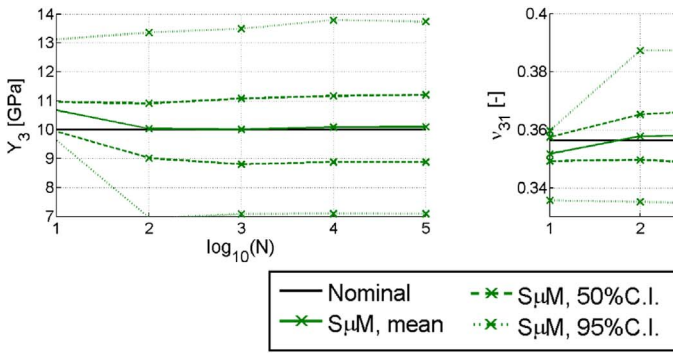
Fig. 7. Convergence plots of the random elastic *moduli* of CB (green lines): Mean values and confidence intervals of the axial *modulus* Y_3 (on the left) and of the lateral contraction ratio ν_{31} (on the right) as a function of the number of realizations. Black lines depict the nominal values. Subscripts refer to the frames depicted in Fig. 3. (For interpretation of the references to color in this figure legend, the reader is referred to the Web version of this article.)

Table 3
Elastic *moduli* of cortical bone: *nominal* values and statistics (resulting from $N = 10^5$ realizations) of the *stochastic* model.

Elastic *moduli*	$Y_1(\equiv Y_2)$	Y_3	G_{12}	$G_{13}(\equiv G_{23})$	$\nu_{12}(\equiv\nu_{21})$	ν_{13}	ν_{31}
Units	$[GPa]$	$[GPa]$	$[GPa]$	$[GPa]$	$[-]$	$[-]$	$[-]$
Nominal model	7.84	10.00	2.94	3.12	0.333	0.280	0.356
SμM of ($\overline{TMD}$, HP)							
Mean value	7.91	10.10	2.97	3.15	0.336	0.279	0.358
Δ_{rel}^N	-0.01	-0.01	-0.01	-0.01	-0.009	0.003	-0.003
Standard deviation	1.55	1.71	0.63	0.64	0.027	0.016	0.014
Dispersion ($[-]$)	0.20	0.17	0.21	0.20	0.080	0.056	0.039
25% quantile	5.50	7.49	1.99	2.15	0.296	0.252	0.336
75% quantile	8.93	11.20	3.39	3.57	0.353	0.290	0.366
5% quantile	6.81	8.88	2.52	2.70	0.317	0.268	0.348
95% quantile	10.57	13.07	4.06	4.24	0.383	0.304	0.382
2.5% quantile	5.11	7.09	1.83	1.98	0.292	0.247	0.333
97.5% quantile	11.15	13.73	4.30	4.47	0.394	0.307	0.388

Table 4
Mean values of the base coefficients (see Appendix C) of the random elasticity tensors of MF, US and CB.

Coeffs of $[\mathbb{C}_*] \in$ Iso	$c_1(\equiv 3 \times K)$				$c_2(\equiv 2 \times G)$
units	$[GPA]$				$[GPA]$
$\hat{\mu}_{[\mathbb{C}_{MF}]}^N$	27.701				8.016

Coeffs of $[\mathbb{C}_*] \in$ TI$(\mathbf{e}_3)$	c_1	c_2	c_3	c_4	c_5
units	$[GPA]$	$[GPA]$	$[GPA]$	$[GPA]$	$[GPA]$
$\hat{\mu}_{[\mathbb{C}_{US}]}^N$	15.734	19.334	9.542	7.392	7.421
$\hat{\mu}_{[\mathbb{C}_{CB}]}^N$	14.382	16.890	8.499	5.944	6.292

Table 5
Dispersions of the random elasticity tensors of MF, US and CB.

$\hat{\delta}_{[\mathbb{C}_{MF}]}^N$	$\hat{\delta}_{[\mathbb{C}_{US}]}^N$	$\hat{\delta}_{[\mathbb{C}_{CB}]}^N$
0.2033	0.1265	0.1435

$$\mathscr{P}_S([\mathbb{c}]) := \sum_{i=1}^{N_S} \frac{\text{Tra}([\mathbb{c}]^T [\mathbb{b}_i])}{[\mathbb{b}_i]_F^2} [\mathbb{b}_i] , \quad E_S([\mathbb{c}]) := \frac{\|\mathscr{P}_S([\mathbb{c}]) - [\mathbb{c}])}{\|[\mathbb{c}]\|_F} ,$$

(3.3)

where Tra is the trace operator, $[\star]^T$ is the transpose operator and N_S

designates the number of necessary and sufficient elements of the orthogonal base (but generally non orthonormal) $\{[\mathbb{b}_1], [\mathbb{b}_2], ..., [\mathbb{b}_{N_S}]\}$ for the complete definition of a symmetry class. The index $E_S([\mathbb{c}])$ in Eq. (3.3) is suitable to measure how good those assumptions are. Actually, it measures the difference between the actual, anisotropic elastic tensor $\mathbb{c}$ and its orthotropic/transversely isotropic approximations (calculated as the projection of $E_S([\mathbb{c}])$ onto the orthotropic/transversely isotropic symmetry class).

Distances $E_{TI}(*)$ and $E_O(*)$ in the FEM and FFT simulations of the 35 RVEs are depicted in Fig. 8.

Since the value of $E_S([\mathbb{c}])$ is in the interval [0, 1], it represents a measure of the relative distance of the matrix $[\mathbb{c}]$ to a element of the class of material symmetry S. Moreover, since the symmetry class O includes the one of TI, it turns out that $E_O([\mathbb{c}]) \le E_{TI}([\mathbb{c}])$. For both methods, the mean values of $E_{TI}(*)$ and of $E_O(*)$ are about 2% and 1.5%, respectively. The FFT estimation generally returns slightly more anisotropic tensors. In both methods, highest errors are observed in the RVE #21 ($E_{TI}(*) \sim 12\%$ and $E_O \sim 4\%$), which is the most porous RVE (HP>20%), and then in RVEs #35 (HP = 15.5%) and #6. These RVEs are shown in Fig. 9.

Base coefficients and relevant elastic *moduli* of the projection $\mathscr{P}_{TI}([\mathbb{c}])$ are reported in Tables 8 and 9 given in Appendix E.

Relative differences between the elastic *moduli* provided by the two methods are shown in Fig. 10 for which the relative error has been introduced:

$$RE_1(y) = \frac{y^{\mu FE} - y^{\mu FFT}}{y^{\mu FFT}}.$$

(3.4)

Lowest differences (most of time smaller than 5%) are observed for the axial *modulus* Y_3 and contraction ratio ν_{31}. Concerning this latter, the highest difference is found in RVE #6 (about 6%). Relative differences in the axial *moduli* Y_1 and contraction ratios ν_{13} and ν_{12} are smaller than 10% excepting the RVE #35. Shear *moduli* G_{13} and G_{12} show differences smaller than 20% on all RVEs expect for RVEs #21 and #35. The high differences observed between μFE and μFFT results in the RVEs #21, #35 and #6 could be explained by the fact that they present big pores on their boundaries. This circumstance could introduce a big approximation in the periodic boundary displacement considered by the FFT method.

3.3.1. Computational time

From the point of view of computational time, the μFE model, despite its simplified representation of the RVEs, takes longer than the μFFT model. On a standard desktop computer, μFE simulations last about half an hour per RVE whereas μFFT simulations only a few minutes.

The computational time required to obtain the solution of the stochastic micromechanical model includes building the databases of HP and average TMD (step 2 of section 2.7.2) – some minutes (less than 7 min) on a recent standard desktop computer – and performing the micromechanical simulations (section 2.7.3) – some hours (less than 2 h).
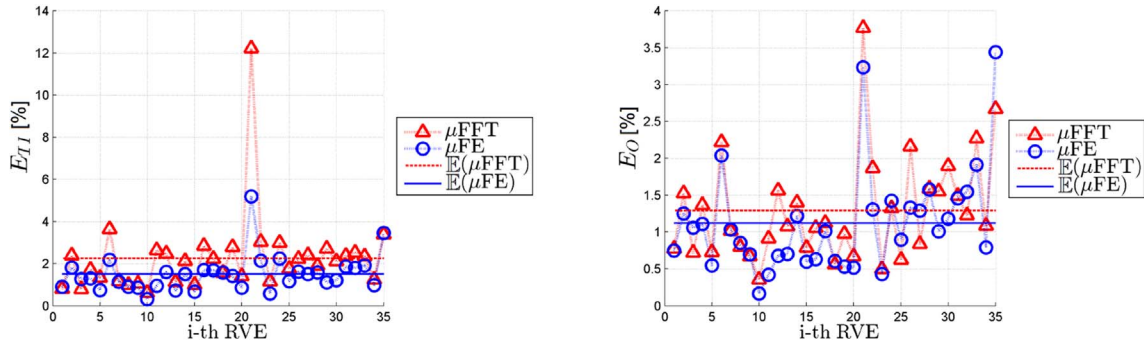
Fig. 8. Distance of the anisotropic elasticity tensors (see Eq. (3.3)/2) of the RVEs obtained by means of the μFFT and μFE models from transverse isotropy (on the left) and orthotropic (on the right) symmetry classes.
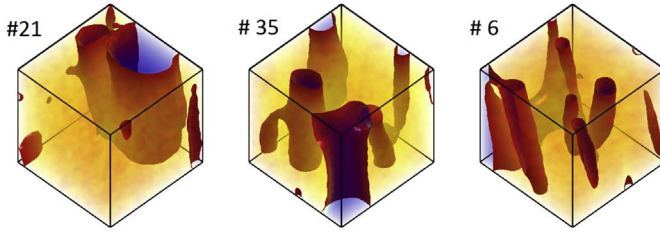

Fig. 9. Reconstruction of the most anisotropic RVEs.

3.4. Validation of the SμM of cortical bone: by comparison with the μFE and μFFT estimates

In this subsection, the results of the stochastic micro-mechanical model will be compared with the approximations given by the FEM and FFT methods. Firstly, a RVE-wise analysis of the differences between the FFT and FEM approximations will be presented, then the FEM and FFT results will be compared with the bounds defined by the confidence intervals and regions of the model.

RVE-wise distance from FEM and FFT estimations. Each CB realization of the stochastic micro-mechanical model is the result of the application of the micro-mechanical model to a fictitious, idealized CB-RVE consisting in the 2-phase defined by a specific assignation of the couple ($\overline{\text{TMD}}$,HP). In Fig. 11, we report the relative differences between the finer estimations (FEM, FFT) of the database of 35 RVEs and the realizations of the SμM model corresponding to the real couple ($\overline{\text{TMD}}$,HP) associated to each RVE. For this figure, the relative errors have been introduced:

$$RE_2(y) = \frac{y^{\mu\text{FE}} - y^{\text{S}\mu\text{M}}}{y^{\text{S}\mu\text{M}}}, \quad RE_3(y) = \frac{y^{\mu\text{FFT}} - y^{\text{S}\mu\text{M}}}{y^{\text{S}\mu\text{M}}}. \tag{3.5}$$

Note that the mean values of the axial *modulus* Y_3 and the lateral contraction ratio ν_{31} are respectively given by $\mathbb{E}(RE_2(Y_3^{\mu\text{FE}})) = 0.5668$, $\mathbb{E}(RE_2(Y_3^{\mu\text{FFT}})) = -0.1528$, $\mathbb{E}(RE_3(\nu_{31}^{\mu\text{FFT}})) = 0.0047$ and $\mathbb{E}(RE_3(\nu_{31}^{\mu\text{FFT}})) = 0.6554$ (see Fig. 11). Analogous results are obtained for the other elastic *moduli*.

3.5. Comparison of the methods

Relative differences between the μFE and μFFT estimates of the elastic *moduli* are reported in Table 6. It can be noticed that, even including the RVEs #21, #35, and #6 (for which the highest differences can be observed), the differences between the two models remain often quite limited. In particular, the difference is (1) negligible (<2%) for Y_3 and ν_{31}, (2) quite small (6%) for Y_1, Y_2, G_{13}, G_{23}, ν_{12} and ν_{13} and (3) noticeable for G_{12} (>10%). The origin of these differences, especially with respect to the contraction ratios and shear *moduli,* can have various interpretations. First, the two models are based on different representations of the heterogeneous microstructure of the RVEs.

Whereas the μFFT model accounts for voxel-wise heterogeneity of the RVE and each voxel inherits its elastic properties based on its own GL (see Sec. 2.10), the μFE model considers a (small) number of homogeneous (sub)regions in the solid matrix and all the FEs inherit the elastic properties of the region that they belong to (see Sec. 2.9). Moreover, the two methods do not solve the same homogenization problem. Indeed, the μFE model solves BVPs with prescribed homogeneous strain on the boundary (*i.e.* $\mathbf{u}(x) = \mathbf{E}^*x$ for all $x \in \partial\Omega$) whereas the μFFT model solves BVPs with prescribed periodic strain (*i.e.* $\mathbf{u}(x) - \mathbf{E}^*x$ periodic for all $x \in \partial\Omega$). Eventually, it should be pointed out that the μFFT method could be affected by the mesh density (here 50^3 points).

Another way to evaluate the relative difference of the estimates of elastic *moduli* is reported in Table 7. From Table 7, we observe that generally the error committed approximating the FEM model with the SμM model is lower than the FFT counterpart. The relative distance from the FEM-approximation is lower than 4% for each elastic *modulus*. Except for G_{12}, $G_{13}G_{23}$ and ν_{12}, the most of elastic *moduli* are not very distant from the FFT (about 5%).

3.6. Accuracy of the stochastic model

In the previous subsection, we underlined the average global distance of the set of RVE-wise predictions of the stochastic model. In this section, we want to put this distance in the right perspective. For this reason, in Fig. 12, we plot the estimation of elastic *moduli* of the calibration subset of RVEs by FEM, FFT and SμM as function of the common information ($\overline{\text{TMD}}$,HP), against the background represented by the transformation of the confidence region at 50%, 95% and 99% of the SμM model driven by ($\overline{\text{TMD}}$,HP). The 95% confidence region of the stochastic model is able to envelope the most of the FEM and even the FFT estimates of the calibration dataset. Similarly, the 50% confidence region contains approximately the 50% results of the control set. Note that the input parameters ($\overline{\text{TMD}}$ and HP) are confined in a rectangular region [0, 25] % for the HP and [0.95, 1.05] g/cm^3 for the $\overline{\text{TMD}}$ (see Fig. 5 for a complete picture). The range of the HP occupies almost one fourth of the maximal one [0,1], the TMD one instead, just a small portion of [0, +∞) g/cm^3. On the one hand, the variation of HP in its range of measure would produce a maximal variation of Y_3 in the range [8,11] GPa and ν_{13} in [0.35, 0.37] (keeping the $\overline{\text{TMD}}$ fixed to its mean value). On the other hand, assigning the HP its mean value, the maximal variation of the $\overline{\text{TMD}}$ on its range of measure would produce a variation of Y_3 in the range of [6,16] GPa and ν_{13} in [0.32, 0.4]. According to this reasoning, we can conclude that the $\overline{\text{TMD}}$ parameter is much more important than the HP parameter in the estimation of the elastic *moduli*. Note that Fig. 12 allow to follow the behaviour of each elastic *modulus* with respect to each parameter HP and TMD independently of one another. In particular, black lines describe the variations of the elastic *moduli* with respect to either HP or $\overline{\text{TMD}}$ while keeping fixed the other parameter to its mean value. Analogous results are obtained for the others elastic
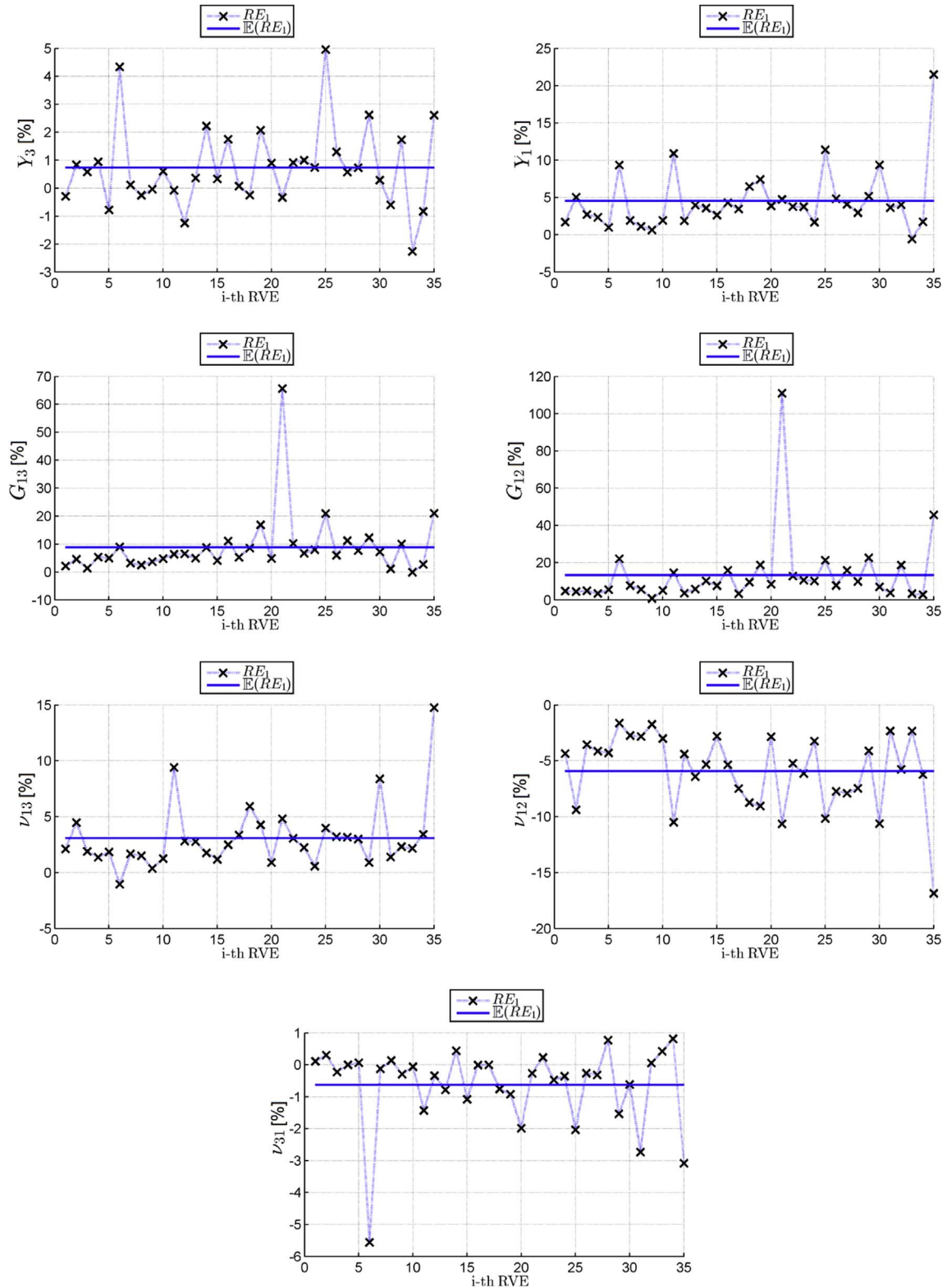
Fig. 10. Elastic *moduli* of cortical bone. Relative differences between μFE and μFFT estimations on individual RVEs (crosses) and average differences (solid lines).

moduli.

Fig. 12 highlights also that the most of the worst approximations (*i.e.* #21 with HP 20% and #35 with HP 15%), being very close to the boundary of the 95% confidence region, could be considered outliers which are results outside the overall pattern of the distribution.

The same figure also shows how the elastic *moduli* are differently influenced by the $\overline{\text{TMD}}$ and HP. More specifically, the elastic *moduli* are

more influenced by the $\overline{\text{TMD}}$ than the HP. Indeed, the intersections between the 99% confidence region and the two parametric study (two thin black lines) for the $\mu(\text{HP})$-fixed study $\mu(\overline{\text{TMD}})$-fixed line gives one insight of the difference. For each parametric study, the minimum and maximum values of the elastic *modulus* can be estimated and the gap (max-min) of these values has been be compared. The highest gap in the *moduli* of Y_1, Y_3, G_{31}, G_{12} and ν_{31} is attained for the $\mu(\text{HP})$-fixed study

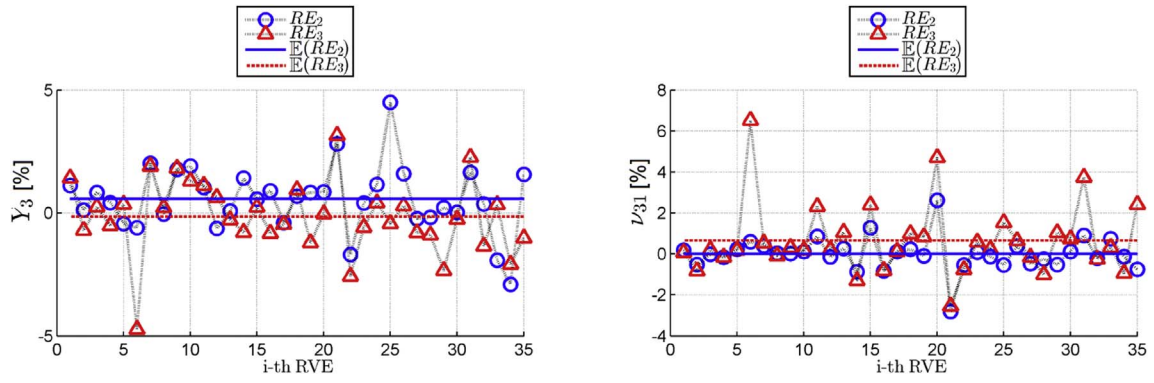**Fig. 11.** Relative differences (see Eq. (3.5)) of the FEM and FFT estimates from the SμM model. Axial *modulus* in the direction of bone axis (Y_3) and lateral contraction ratio (ν_{31}).

(variation of the $\overline{TMD}$). Otherwise, the highest gap in the *moduli* ν_{12} and ν_{13} appears in the $\mu(\overline{TMD})$-fixed study.

This remark allows to observe that the variations Y_1, Y_3, G_{31}, G_{12} and ν_{31} *moduli*, in statistical terms, are mainly implied by that of $\overline{TMD}$. In other terms, the value of $\overline{TMD}$ represents the main determinant of the elastic *moduli* listed above, because the estimates resulting from

considering the same level of HP ($\mu(HP)$) for every RVEs would not differ significantly from that which considers each RVE to have a different value of HP. This constat is based on the confidence region obtained *via* the SμM model based on minimal information about the variables ($\overline{TMD}$,HP) and could not be directly given by the very exiguous database of the calibration dataset.
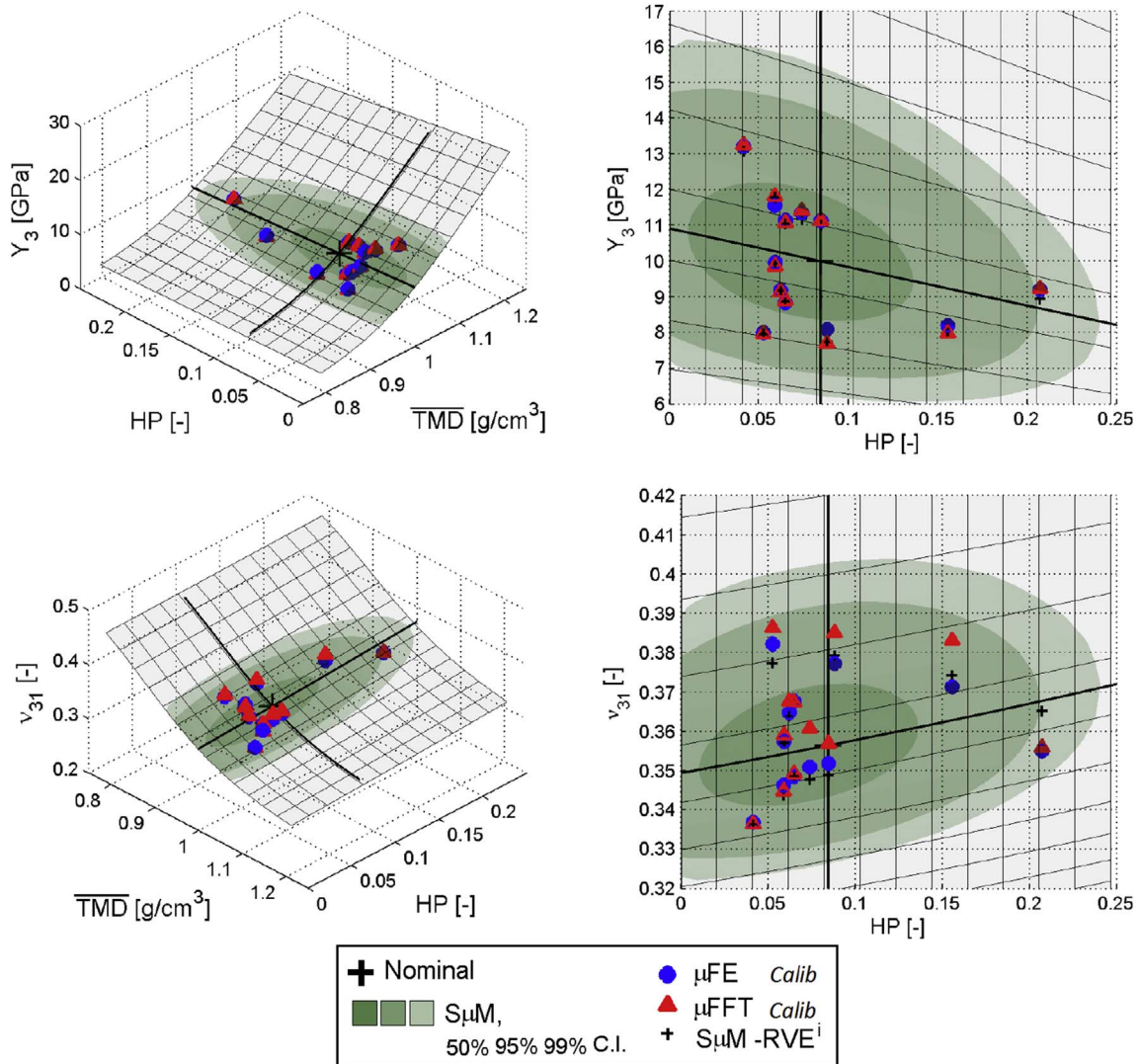
Fig. 12. Comparison of the estimation of the elastic *moduli* as function of TMD and HP measure: (1) parametric study (gray surface); (2) region of the surface corresponding to the 50%, 95% and 99% confidence intervals of the stochastic model (green area with multiple transparencies); (3) estimations of the 12 RVEs by μFE (blue dots); (4) FFT (red triangles); (5) Nominal model (+). (For interpretation of the references to color in this figure legend, the reader is referred to the Web version of this article.)

Table 6
Average relative differences between the μFE and μFFT estimations of the elastic *moduli* of cortical bone.

Elastic *moduli*	Y_1	Y_2	Y_3	G_{12}	G_{13}	G_{23}	ν_{12}	ν_{13}	ν_{31}
$\sqrt{\dfrac{\mathbb{E}\left((y^{\mu FE}-y^{\mu FFT})^2\right)}{\mathbb{E}\left((y^{\mu FFT})^2\right)}}$ [%]	5.1	5.1	1.5	13.6	6.5	9.6	7.22	3.93	1.43

Table 7
Stochastic model of cortical bone approximation to _FE and _FFT estimations of elastic properties.

Elastic *moduli*	Y_1	Y_2	Y_3	G_{12}	G_{13}	G_{23}	ν_{12}	ν_{13}	ν_{31}
$\sqrt{\dfrac{\mathbb{E}\left((y^{\mu FE}-y^{S\mu M})^2\right)}{\mathbb{E}\left((y^{S\mu M})^2\right)}}$ [%]	3.0	2.6	1.4	3.2	2.7	3.3	3.46	2.54	0.83
$\sqrt{\dfrac{\mathbb{E}\left((y^{\mu FFT}-y^{S\mu M})^2\right)}{\mathbb{E}\left((y^{S\mu M})^2\right)}}$ [%]	5.0	5.7	1.5	11.7	7.0	10.1	8.25	4.45	1.82

Moreover, Fig. 13 shows the results of the FFT, FEM and SμM estimations for the whole dataset (calibration and control) and the confidence intervals of the stochastic model. As evidenced by this figure, the 95% confidence interval covers, not only, the 95% of the FEM and FFT estimations for the calibration dataset (*Calib* dataset), but also the control dataset (*Ctrl* dataset). This result shows that a stochastic model based on minimal information about two measures ($\overline{TMD}$,HP) is able to reproduce the variability of a studied region of the cortical bone (at such a distance by the periosteum) and to capture finer estimation by FE and FFT methods for the most of elastic *moduli* (except for G_{12}).

The fact that the aforementioned micromechanical models perform more weakly with respect to G_{12} than with respect to the other elastic properties, is actually well known in the literature (see *e.g.* Hellmich et al. (2004a)). A corresponding remedy has been proposed in terms of a more refined micromechanical model which explicitly considers the morphological nature of mineralized collagen fibrils embedded in an extrafibrillar matrix (see *e.g.* Fritsch and Hellmich (2007)). Nevertheless, we believe that the difference in the estimation of the coefficient G_{12} in our scenario is rather related to the most evident feature in which these approximations differ from one another, *i.e.* the morphological approximation of the Havers-Volkmann canal system of the *Calib* dataset. Indeed, the actual *Calib* dataset contains some cortical

bone-volume elements (RVE number 21 and 35 in Fig. 9) that could not be really considered as representative and in statistical terms their contribution in this error can not be cancelled due to the small sample number in the dataset (even extending the *Calib* dataset to the *Ctrl* dataset, see the section on the results). More accurate description of the sub-ultrastructure scales could certainly improve the common description of the three approximations (micromechanical, FEM and FFT) at the scale of the cortical bone.

3.7. Remarks on the propagation of uncertainty through the scales

A first proof of concept of the propagation of uncertainty was proposed in Sansalone et al. (2016) in which the authors have investigated the propagation of uncertainty related to bone composition through the scales. In Sansalone et al. (2016), probability density functions were constructed only for the volume fractions using the MaxEnt principle and experimental data at the voxel scale. By contrast, in this study we focused on the $\overline{TMD}$ and RVE-scale data. (See below a discussion on the spatial scale of the experimental data.). Moreover, whereas the homogenization procedure *via* the finite elements method is relatively usual, it is not the case for the Fast Fourier Transform (FFT) method, in particular, in the biological context. For this study, this method is particularly relevant. Indeed, one of the main advantages of FFT-based methods is that they directly use numerical images of the microstructure, and all fields of interest (stress, strain, …) are computed at every pixel of the image. Another important feature is that the required CPU time is roughly proportional to the size of the image (in pixels or voxels). In addition, with respect to our previous work (Sansalone et al., 2016), in the actual work some sensible modifications have been done. In this previous work, the transverse anisotropy of the ultrastructure (step 2 of the homogenization procedure) resulted from the application of the Mori-Tanaka scheme to the cylindrical inclusions of isotropic collagen in isotropic mineral foam. In the actual work, the elastic model of the collagen has been modelled itself as transversely isotropic. Evident differences in the results at CB scale can be seen comparing Table 3 of the actual work and Table 2 in Sansalone et al. (2016). An instance of the differences is given by the axial *modulus* in the direction of bone axis Y_3 between the present work (see Fig. 13) and the one of Sansalone et al. (2016) (see Fig. 10 in this work).

Moreover, the protocol for gathering information from μCT images and setting-up the stochastic model has been modified with respect to that used in Sansalone et al. (2016). The actual protocol could appear only slightly different from the previous one but the results descending from these modifications motivate us for the extended treatment given in subsection 2.2 and 2.3 of section 2 "Material and methods". In the
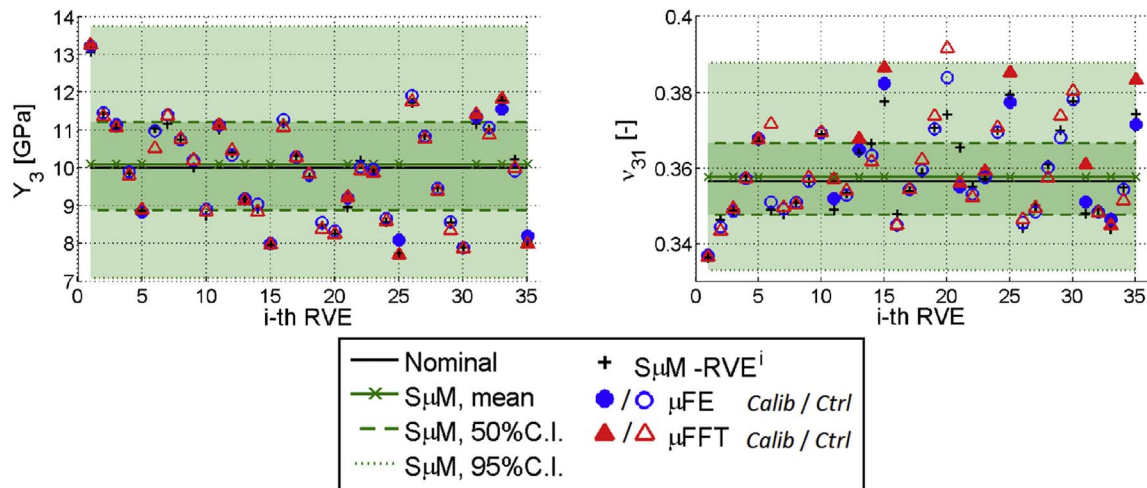

Fig. 13. Axial *modulus* in the direction of bone axis Y_3 and lateral contraction ratio ν_{31}.

previous protocol the statistics (mean value and dispersion) on the tissue mineral density (TMD) were estimated on the whole set (named as "global database" in Sansalone et al. (2016)) of solid voxels belonging to all cortical-bone volume elements (CB-VE). In this description, the TMD had been considered as a measure at a voxel-scale ($10\,\mu m$). In the actual protocol, each CB-VE has been treated first independently from one another and then the mean value of TMD (denoted $\overline{\text{TMD}}$) obtained on each CB-VE has been considered as the database for evaluating the statistical information of the stochastic model. This variation in the settings of the stochastic protocol is translated in a huge difference in the confidence intervals easily observable by comparing Fig. 13 of the actual work and Fig. 10 in Sansalone et al. (2016). In the actual protocol, the estimated confidence intervals of elastic coefficients fit much better with those obtained with other – more accurate – homogenization techniques (FEM and FFT).

3.8. Remarks on the range of gray scale values

It is probable that a modern micro-CT scanner working with a range of gray scale values higher than 8 bits, typically 16, could be used for this study. Nevertheless, we are not sure that choosing images having better quality could have a sensible impact on the final prediction of our stochastic model. Better images, for instance, can have a direct impact on the selection of the separation threshold given by the parameter q (see subsection 2.2) between the porous and solid voxels and specifically on the range of the TMD. Despite that, our study shows that the overall properties of a CB-volume element of cortical bone is strongly correlated to the mean value of TMD (denoted $\overline{\text{TMD}}$) and not to the individual value (that could be establish with less accuracy by using 8 bit-images). A preliminary study that we performed before setting-up q (but out of the topic of this work) on the same dataset shows that it would be necessary a variation of 23% of q (27% if we consider the corresponding value of mineralization TMD(q)) to perturb the estimation of $\overline{\text{TMD}}$ of barely 0.65% and finally the estimated elastic coefficients of less than 3% (1.34% for Y_3 and 2.82% for ν_{13}).

4. Conclusion and perspectives

In this work, a stochastic model of cortical bone based on the theory of micromechanical homogenization and the MaxEnt principle applied to a very exiguous information on TMD and HP measures estimated from μCT, has been presented. It has been shown that the information on the first two moments (mean and dispersion) for both TMD and HP measures at the resolution of scale (RVE) is sufficient for setting geometric-idealized model, able to compete with finer estimations. At millimeter scale, the choice of the Mori-Tanaka scheme for the homogenization with cylindrical inclusions allows to reproduce the same degree of anisotropy that the detailed models. Indeed, it has been shown that the transverse isotropic class of materials is the relevant model, since it covers the 98% of the effective tensor estimated with both FE and FFT models. The class of orthotropic materials, benefiting of 4 more parameters, improve only of 1% the performances of the transverse isotropic class. Again, the stochastic model, contrarily to the FE and FFT methods applied to the same database, is able to determine confidence intervals and regions. These remarks allow to consider the SμM as the first main benchmark to be applied before any deeper analysis on bone tissues. Furthermore, the confidence regions estimated with this method provides the probability landscape of the main six elastic *moduli* and represents a tool *a priori* for the interpretation of results given by other homogenization methods. Finally, our simple SμM based on the HP and mean value of the TMD at the millimeter scale allows to verify that the most relevant factor in the estimation of elastic properties of cortical bone is given by the $\overline{\text{TMD}}$. Nevertheless, in terms of perspectives, the current model based on the ($\overline{\text{TMD}}$,HP) at millimeter RVE scale can be ameliorated including other interesting features as the correlation length of the main random variables ($\overline{\text{TMD}}$,HP) and other statistical constraints allowing to improve the likelihood of the probability density function determined by the MaxEnt principle to the experimental one.

A. Overview on the homogenization

Homogenization is concerned with the problem of computing the effective mechanical properties of an heterogeneous medium. Restricting our attention to linearly elastic materials occupying a representative volume element (RVE), the problem can be stated as follows.

Let Ω be the region of the three-dimensional space occupied by the RVE, $\mathfrak{c}(x)$ ($x \in \Omega$) the fourth-order elasticity tensor field describing the point-wise elastic properties of the heterogeneous material. Thus, the point-wise constitutive relation reads:

$$\mathbf{S}(x) := \mathfrak{c}(x): \mathbf{E}(x), \tag{A.1}$$

where the symbol ":" between two tensors denotes a double contraction of adjacent indexes of any couple of tensors, $\mathbf{S}(x)$ is the second-order *stress tensor* field and $\mathbf{E}(x)$ is the second-order *infinitesimal strain tensor* field, that is the symmetric part of the gradient of the *displacement* field $\mathbf{u}(x)$:

$$\mathbf{E}(x) := Sym(\nabla\mathbf{u}(x)) \equiv \frac{\nabla\mathbf{u}(x) + (\nabla\mathbf{u}(x))^T}{2}. \tag{A.2}$$

where ∇ is the gradient operator, $(\star)^T$ is the transpose operator and $Sym(\star)$ is the symmetry operator as defined by the relation (A.2).

Moreover, let $\mathbf{S}^*$ and $\mathbf{E}^*$ be the spatial averages of $\mathbf{S}(x)$ and $\mathbf{E}(x)$, respectively, that is:

$$\mathbf{S}^* := \langle \mathbf{S}(x) \rangle_\Omega, \quad \mathbf{E}^* := \langle \mathbf{E}(x) \rangle_\Omega, \quad \langle * \rangle_\Omega := \frac{1}{|\Omega|} \int_\Omega [*](x)\,dx. \tag{A.3}$$

Then, the *homogenization problem* consists in looking for a fourth-order elasticity tensor $\mathfrak{c}^*$ such that:

$$\mathbf{S}^* = \mathfrak{c}^*: \mathbf{E}^*, \quad \text{for all admissible pair } (\mathbf{S}^*, \mathbf{E}^*) \tag{A.4}$$

In the above statement, admissibility of average stress and strain refers to the underlying stress and strain fields which are required to be the solution of the boundary value problem (BVP) at the RVE scale:

$$\begin{cases} \nabla \cdot \mathbf{S}(x) = 0, & \forall\, x \in \Omega, \\ f\,[\mathbf{u}(x), \mathbf{t}(x)] = 0 & \forall\, x \in \partial\Omega \end{cases} \tag{A.5}$$

where $\nabla\cdot$ is the divergence operator, $\mathbf{t}$ is the boundary traction, $\partial\Omega$ is the boundary of the domain Ω and f is an operator which allows to specify the boundary conditions. The equation in the system (A.5) is known as the *equilibrium equation* of elasticity (by neglecting body forces) at which is associated with boundary conditions.

The expression of the boundary conditions in Eq. (A.5) is intentionally left implicit because it depends on the specific BVP (*e.g.* prescribed displacement, traction, periodic, …) to be solved in order to compute $\mathfrak{c}^*$.

Hereinafter, Kelvin representation (denoted by brackets) will be widely used for representing stress, strain and elasticity tensors (see Appendix B). Thus, second-order stress and strain tensors will be represented as 6-dimensional vectors and elasticity tensors as 6×6 symmetric matrices. For instance, the Kelvin form of the homogenized elastic law in Eq. (A.4) reads:

$$
\begin{bmatrix} S_{11}^* \\ \vdots \\ \sqrt{2}\, S_{12}^* \end{bmatrix} = \begin{bmatrix} C_{1111}^* & \cdots & \sqrt{2}\, C_{1112}^* \\ \vdots & \ddots & \vdots \\ \sqrt{2}\, C_{1112}^* & \cdots & 2\, C_{1212}^* \end{bmatrix} \cdot \begin{bmatrix} E_{11}^* \\ \vdots \\ \sqrt{2}\, E_{12}^* \end{bmatrix} .
$$

(A.6)

It is worth noting that Eq. (A.6) shows clearly that $\mathfrak{c}^*$ is fully determined from 6 linearly independent pairs ($[\mathbf{S}^*]$, $[\mathbf{E}^*]$).

A.1. Continuum micromechanics

Continuum micromechanics provides estimates of the homogenized elasticity tensor $\mathfrak{c}^*$ of heterogeneous materials with microstructure of matrix-inclusion type. We recall here the main ingredients of continuum micromechanics and refer to Suquet (1997); Nemat-Nasser and Hori (1999); Zaoui (2002) for further details. Continuum micromechanics is based on the solution of the matrix-inclusion problem provided by Eshelby in the fifties (Eshelby, 1957). Eshelby's solution describes the elastic fields (strain, stress) generated by one ellipsoidal inclusion in an infinite isotropic elastic matrix under homogeneous strain/stress boundary conditions at infinity. Eshelby's solution was further extended to inclusions of different shapes, including cylinders and penny-shaped cracks (Laws, 1985), and to anisotropic matrices (Laws, 1977). General formulæ for dealing with ellipsoidal inclusions in an anisotropic solid can be found in Suvorov and Dvorak (2002).

Micromechanical homogenization–*i.e.* homogenization theory based on continuum micromechanics– can estimate the homogenized elasticity tensor of a RVE made up of several phases with different distributions and shapes, whether or not organized in a matrix/inclusion-like microstructure. The homogenized elasticity tensor turns out to be a weighted sum over the phases:

$$
\mathfrak{c}^* = \sum_r \phi_r\, \mathfrak{c}_r : \mathfrak{a}_r ,
$$

(A.7)

where ϕ_r is the volume fraction of phase r, $\mathfrak{c}_r$ and $\mathfrak{a}_r$ are the fourth-order *elasticity* and *localization* tensors of phase r, respectively. Note that the following condition is required $\sum_{r=0}^{(N_p-1)} \phi_r = 1$ where $(N_p - 1)$ is the total number of phases.

The *localization* tensor resumes the relation between the microscopic strain field $E(x)$ and the macroscopic strain $\mathbf{E}^*$, *i.e.* $\mathbf{E}(x) = \mathfrak{a}_r(x) : \mathbf{E}^*$.

It can be shown that the expression of $\mathfrak{a}_r$ reads (see for instance Hellmich et al. (2004a)):

$$
\mathfrak{a}_r = (\mathfrak{i} + \mathfrak{p}_r^0 : (\mathfrak{c}_r - \mathfrak{c}_0))^{-1} : \left[\sum_{s=0}^{N_p-1} \phi_s (\mathfrak{i} + \mathfrak{p}_s^0 : (\mathfrak{c}_s - \mathfrak{c}_0))^{-1} \right]^{-1} ,
$$

(A.8)

where $\mathfrak{c}_0$ represents the elasticity tensor of the matrix phase embedding all other phases; $\mathfrak{i}$ is the fourth-order symmetric identity tensor (with $\mathfrak{i}_{ijhk} = 1/2\,(\delta_{ih}\delta_{jk} + \delta_{ik}\delta_{jh})$ where δ_{ij} are the components of the Kronecker operator); $\mathfrak{p}_r^0$ is the so-called Hill tensor of the phase r embedded in the effective matrix. The expression of this latter depends on the shape of the phase r and on its materials properties. Explicit expressions of $\mathfrak{p}_r^0$ have been developed in some special cases (*e.g. cylindrical* or *spherical* inclusions in *transversely isotropic* matrix) but, in general, the Hill tensor has to be computed numerically (Suvorov and Dvorak, 2002).

The choice of the value of $\mathfrak{c}_0$ leads to different estimates of $\mathfrak{c}^*$. Among others, two estimates are relevant in the context of this paper. The Mori-Tanaka (MT) estimate (Nemat-Nasser and Hori, 1999) is well suited when the material microstructure is made up of uniformly dispersed inclusions in a homogeneous matrix. In this case, the effective matrix is an actual, well identified phase and therefore $\mathfrak{c}_0 = \mathfrak{c}_{matrix}$. Then, the MT estimate of $\mathfrak{c}^*$ can be readily computed from Eq. (A.7). The Self-Consistent (SC) estimate (Nemat-Nasser and Hori, 1999) is well suited when no actual matrix can be identified but the microstructure is rather made of interpenetrating (continuous or discontinuous) phases. In this case, the effective matrix is assumed to be the homogenized material itself and therefore $\mathfrak{c}_0 = \mathfrak{c}^*$. It follows that the SC estimate of $\mathfrak{c}^*$ shall be computed iteratively since $\mathfrak{c}^*$ appears on both sides of Eq. (A.7).

Looking at the structure of bone at each scale considered in this study, the SC scheme can be used to estimate the effective elasticity tensor of the MF, then the MT scheme to estimate those of the US and of the CB. The expression of the SC estimate of $\mathfrak{c}^*$ for a two-phase material such as the MF reads:

$$
\mathfrak{c}^* = [\phi_0 \mathfrak{c}_0 : (\mathfrak{i} + \mathfrak{p}_0^{SC} : (\mathfrak{c}_0 - \mathfrak{c}^*))^{-1} + \phi_1 \mathfrak{c}_1 : (\mathfrak{i} + \mathfrak{p}_1^{SC} : (\mathfrak{c}_1 - \mathfrak{c}^*))^{-1}]
$$
$$
: [\phi_0 (\mathfrak{i} + \mathfrak{p}_0^{SC} : (\mathfrak{c}_0 - \mathfrak{c}^*))^{-1} + \phi_1 (\mathfrak{i} + \mathfrak{p}_1^{SC} : (\mathfrak{c}_1 - \mathfrak{c}^*))^{-1}]^{-1} ,
$$

(A.9)

where the subscripts 0 and 1 refer to the matrix and inclusion phases, respectively. Moreover, the expression of the MT estimate of $\mathfrak{c}^*$ for a two-phase material such as the US and the CB reads:

$$
\mathfrak{c}^* = [\phi_0\, \mathfrak{c}_0 : \mathfrak{i} + \phi_1\, \mathfrak{c}_1 : (\mathfrak{i} + \mathfrak{p}_1^{MT} : (\mathfrak{c}_1 - \mathfrak{c}_0))^{-1}]
$$
$$
: [(\phi_0\, \mathfrak{c}_0 : \mathfrak{i} + \phi_1\, \mathfrak{c}_1 : (\mathfrak{i} + \mathfrak{p}_1^{MT} : (\mathfrak{c}_1 - \mathfrak{c}_0))^{-1})]^{-1} .
$$

(A.10)

For the sake of synthesis, Eqs. (A.9)–(A.10) have been rewritten more compactly as:

$$g^{sch}(\mathfrak{c}^*; \{\phi_r\}, \{\mathfrak{c}_r\}) = 0, \quad r = 0, ..., N_p - 1,$$ (A.11)

where g^{sch} refers to the application of the scheme *sch* (*i.e.* SC or MT) to the homogenized elasticity tensor $\mathfrak{c}^*$, from ϕ_r and $\mathfrak{c}_r$, the volume fraction and elasticity tensor respectively, of the phase *r*. Note that the application g^{sch} also depends upon the Hill tensor which is computed numerically (Suvorov and Dvorak, 2002).

A.2. Homogenization by finite element method (FEM)

The finite element method (FEM) consists in the solution of a suitable *weak formulation* of the problem defined from Eq. (A.5) for a specific set of boundary conditions (prescribed displacement, traction, periodic, …). More details on this standard technique can be found in Zohdi and Wriggers (2001).

In this work, the boundary condition used in the problem (see Eq. (A.5)) is given by:

$$\mathbf{u} = \mathbf{E}^* \, \mathrm{x} \quad \forall \, \mathrm{x} \in \partial\Omega,$$ (A.12)

where $\mathbf{E}^*$ is a given strain tensor independent of x.

A *weak formulation* is obtained from the equilibrium equations of elasticity and associated boundary conditions (BC). From this formulation, the FEM is used to resolve this problem which leads to the solution in displacement field $\mathbf{u}(\mathrm{x})$. This field displacement allows to determine the strain field $\mathbf{E}(\mathrm{x})$ from Eq. (A.2) and the stress field $\mathbf{S}(\mathrm{x})$ from Eq. (A.1). The effective elastic properties of an heterogeneous RVE is obtained by a judicious choice of six sets of uniform displacements (KUBC, for kinematic uniform BC) boundary conditions following a well-documented procedure (see *e.g.* Zohdi and Wriggers (2001)) that amounts to simulating longitudinal traction tests in every direction. These computations yield a linear system of 36 equations whose the solution forms the components of the elasticity tensor $\mathfrak{c}^*$ which defines the effective elastic properties of an heterogeneous RVE.

The boundary value problem in each RVE was solved with the commercial finite element code Comsol Multiphysics (COMSOL Multiphysics, 2015). The equations of linearized elasticity were discretized on an unstructured mesh of tetrahedral elements with characteristic size *h*. Comsol Multiphysics does not assign stiffness values to each element individually but uses a function which returns the local elastic coefficients at arbitrary coordinates (x_1, x_2, x_3). The shape functions used in the discretized equations of linearized elasticity are Lagrange interpolation polynomials of second degree.

A.3. Homogenization by Fast Fourier Transform (FFT) method

One of the main advantages of Fast Fourier Transform-based methods (Moulinec and Suquet, 1998) presented below is that they directly use numerical images of the microstructure, and all fields of interest (stress, strain, …) are computed at every pixel of the image. Another important feature is that the required cpu time is roughly proportional to the size of the image (in pixels or voxels).

The FFT method is applied to solve the problem (A.5). To this aim, first of all a particular version of the equilibrium equation has to be defined. In general, the FFT method can be performed by means of the assignation of *periodic* boundary conditions to the strain field or to *antiperiodic* condition to the stress field. For simplicity, we describe the case of *periodic* conditions prescribed on the strain field.

As already mentioned, in order to compute the effective elasticity tensor $\mathfrak{c}^*$ of an heterogeneous RVE, 6 problems have to be solved corresponding to 6 linearly independent boundary conditions.

The problem consists in finding the displacement field $\mathbf{u}(\mathrm{x})$ such that:

$$\begin{cases} \nabla \cdot \mathbf{S}(\mathrm{x}) = 0, & \forall \, \mathrm{x} \in \Omega \\ \mathbf{S}(\mathrm{x}) = \mathfrak{c}(\mathrm{x}): \mathbf{E}(\mathrm{x}), & \forall \, \mathrm{x} \in \Omega \\ \mathbf{u}(\mathrm{x}) - \mathbf{E}^* \mathrm{x}, & \text{periodic for all } \mathrm{x} \in \partial\Omega \end{cases}$$ (A.13)

By addition and subtraction of a homogeneous test elasticity tensor $\mathfrak{c}_0$, the problem can be turned in:

$$\mathbf{S}(\mathrm{x}) = \mathfrak{c}_0: \mathbf{E}(\mathrm{x}) + \mathbf{P}(\mathrm{x}) \quad \text{with} \quad \mathbf{P}(\mathrm{x}): = (\mathfrak{c}(\mathrm{x}) - \mathfrak{c}_0): \mathbf{E}(\mathrm{x}).$$ (A.14)

The tensor $\mathbf{P}(\mathrm{x})$ is the so-called *polarization* tensor field. equation (A.14) represents the stress field in a prestressed homogeneous medium. If $\mathbf{P}(\mathrm{x})$ is supposed to be known, the solution of the new problem defined by:

$$\nabla \cdot (\mathfrak{c}_0: \mathbf{E}(\mathrm{x})) = -\nabla \cdot (\mathbf{P}(\mathrm{x})),$$ (A.15)

is given by the strain field defined by:

$$\mathbf{E}(\mathrm{x}) = \mathbf{E}^* - (\mathbf{\Gamma}^0 * \mathbf{P})(\mathrm{x}), \quad \text{or} \quad \mathbf{E}(\mathrm{x}) + \{\mathbf{\Gamma}^0 * [(\mathfrak{c} - \mathfrak{c}_0): \mathbf{E}]\}(\mathrm{x}) = \mathbf{E}^*,$$ (A.16)

where $\mathbf{\Gamma}^0$ is the Green operator for strains associated to the material characterized by the elasticity tensor $\mathfrak{c}_0$. This equation is known as Lippman-Schwinger equation. Moreover, in this equation, the symbol "*" designates the *convolution* operator combined with a double contraction of adjacent indexes of any couple of tensors which is defined by:

$$(\mathbf{\Gamma}^0 * \mathbf{P})(\mathrm{x}): = \int_\Omega \mathbf{\Gamma}^0(\mathrm{x} - \mathrm{y}): \mathbf{P}(\mathrm{y}) dy = \int_\Omega \mathbf{\Gamma}^0(\mathrm{y}): \mathbf{P}(\mathrm{x} - \mathrm{y}) dy.$$ (A.17)

Equation (A.16) can be solved for E(x) by transforming the problem in the Fourier space:

$$\begin{cases} \hat{\mathbf{E}}(\xi) = -\hat{\mathbf{\Gamma}}^0(\xi): \hat{\mathbf{P}}(\xi) \quad \forall \, \xi \neq 0, \\ \hat{\mathbf{E}}(0) = \mathbf{E}^*, \end{cases}$$ (A.18)

where the Fourier transform is denoted by a hat superimposed on the quantity and ξ is the wave vector corresponding to a given period of the distribution in Fourier space.

Equation (A.18) can be stated for any test material –*i.e.* irrespective of the symmetry class of $\mathfrak{c}_0$. However, assuming $\mathfrak{c}_0$ to be the elasticity tensor of an isotropic material, $\hat{\mathbf{\Gamma}}^0$ can be represented as:

$$\hat{\Gamma}^0_{khij}(\xi) = \frac{1}{4\mu^0|\xi|^2}(\delta_{ki}\xi_h\xi_j + \delta_{hi}\xi_k\xi_j + \delta_{kj}\xi_h\xi_i + \delta_{hj}\xi_k\xi_i) - \frac{\lambda^0 + \mu^0}{\mu^0(\lambda^0 + 2\mu^0)}\frac{\xi_i\xi_j\xi_k\xi_h}{|\xi|^4},$$

(A.19)

where λ^0 and μ^0 are the Lamé's coefficients characterizing the elasticity tensor $\mathfrak{c}_0$ of the homogeneous test material, and δ_{ki} is the Kronecker's symbol.

Equation (A.16) is an implicit expression of $\mathbf{E}(x)$ to be solved iteratively. An iterative scheme allows resolving the problem:

$$\begin{cases} [\mathbf{E}(x)]^{(0)} = \mathbf{E}^*, \\ [\mathbf{E}(x)]^{(n+1)} = \mathbf{E}^* - \{\mathbf{\Gamma}^{0*}[\mathbf{P}]^{(n)}\}(x), \quad [\mathbf{P}(x)]^{(n)} = [\mathfrak{c}(x) - \mathfrak{c}_0]: [\mathbf{E}(x)]^{(n)}. \end{cases}$$

(A.20)

At each iteration, four steps are performed:

1. The polarization tensor field $[\mathbb{P}(x)]^{(n)}$ is evaluated in the Fourier space as $[\hat{\mathbf{P}}(\xi)]^{(n)}$;
2. The Fourier problem, defined by:

$$\begin{cases} [\hat{\mathbf{E}}(\xi)]^{(n+1)} = -\hat{\mathbf{\Gamma}}^0(\xi): [\hat{\mathbf{P}}(\xi)]^{(n)} \\ [\hat{\mathbf{E}}(0)]^{(n+1)} = \mathbf{E}^* \end{cases}$$

(A.21)

is solved for $[\hat{\mathbf{E}}(\xi)]^{(n+1)}$;

3. Then, $[\mathbf{E}(x)]^{(n+1)}$ is computed as the inverse Fourier transform of $[\hat{\mathbf{E}}(\xi)]^{(n+1)}$.
4. Eventually, $[\mathbf{S}(x)]^{(n+1)}$ is computed by means of the Hooke law $[\mathbf{S}(x)]^{(n+1)} = \mathfrak{c}(x): [\mathbf{E}(x)]^{(n+1)}$

The above procedure is iterated as long as the current estimate of the stress field does not satisfy the bulk balance and stops when the error, defined as:

$$\varepsilon^{(n)} = \frac{\|\nabla \cdot (\{\mathbf{S}(x)\}^{(n)})\|_{L^2}}{\sqrt{\Omega} \times \langle\{\mathbf{S}(x)\}^{(n)}\rangle_{\Omega \, F}},$$

(A.22)

εbecomes smaller than a fixed threshold. It is worthy observing that, by means of the Parseval identity applied to the stress tensor field $\mathbf{S}(x)^{(n)}$, the value of the error $\varepsilon^{(n)}$ can be estimated already at the previous step with respect of its Fourier transform $\hat{\mathbf{S}}^{(n)}$, as:

$$\varepsilon^{(n)} \equiv \frac{\|(\{\hat{\mathbf{S}}(\xi)\}^{(n)})\xi\|_{L^2}}{\|\hat{\mathbf{S}}(0)^{(n)}\|_F},$$

(A.23)

where L^2 is the Hilbert space whose the norm for all function $f(x) \in L^2$ is defined by the relation:

$$\left\|f(x)\right\|_{L^2} = \left(\int |f(x)|^2 \, dx\right)^{1/2}.$$

(A.24)

B. Kelvin' representation of a fourth-order tensor

The elasticity tensor $\mathfrak{c}$ is defined as a fourth-order tensor in the tridimensional space describing the linear relation between the strain tensor $\mathbf{E}$ and the stress tensor $\mathbf{S}$. This relation takes the form:

$$\mathbf{S} = \mathfrak{c}: \mathbf{E}, \qquad S_{k\ell} = c_{k\ell mn}E_{mn},$$

(B.1)

where the symbol ":" between two tensors denotes a double contraction of adjacent indexes of tensors of rank two and higher.

The 3 symmetry conditions (*minor* and *major*) must be considered on the elasticity tensor $\mathfrak{c}$ (Podio-Guidugli, 2000):

$$c_{k\ell mn} = c_{k\ell nm}, \qquad c_{k\ell mn} = c_{\ell kmn}, \qquad c_{k\ell mn} = c_{mnk\ell}.$$

(B.2)

The second and fourth rank tensors in three dimensions are represented in a Euclidian six-dimensional space as vectors and tensors, respectively. To this end, the representation adopted in this work is called the *Kelvin*'s representation in which the new indexes I et J vary in the set $\{1,...,6\}$ such as $I = (k, \ell)$ and $J = (m, n)$ where the indices k, ℓ, m and n vary in the set $\{1,...,3\}$. The relation between these indices is the following $1 = (1,1)$, $2 = (2,2)$, $3 = (3,3)$, $4 = (2,3)$, $5 = (1,3)$ and $6 = (1,2)$. So, the symmetric matrix $\tilde{\mathfrak{c}}$ associated with $\mathfrak{c}$ is defined *via* these components by:

$$\tilde{\mathfrak{c}}_{IJ} = c_{k\ell mn}.$$

(B.3)

The linear relation between the strain and stress vectors takes the form:

$$
\begin{bmatrix} S_{11} \\ S_{22} \\ S_{33} \\ \sqrt{2}\,S_{13} \\ \sqrt{2}\,S_{23} \\ \sqrt{2}\,S_{12} \end{bmatrix} = \begin{bmatrix} \tilde{c}_{11} & \tilde{c}_{12} & \tilde{c}_{13} & \sqrt{2}\,\tilde{c}_{14} & \sqrt{2}\,\tilde{c}_{15} & \sqrt{2}\,c_{16} \\ \tilde{c}_{21} & \tilde{c}_{22} & \tilde{c}_{33} & \sqrt{2}\,\tilde{c}_{24} & \sqrt{2}\,\tilde{c}_{25} & \sqrt{2}\,c_{26} \\ \tilde{c}_{31} & \tilde{c}_{32} & \tilde{c}_{33} & \sqrt{2}\,\tilde{c}_{34} & \sqrt{2}\,\tilde{c}_{35} & \sqrt{2}\,\tilde{c}_{36} \\ \sqrt{2}\,\tilde{c}_{41} & \sqrt{2}\,\tilde{c}_{42} & \sqrt{2}\,\tilde{c}_{43} & 2\tilde{c}_{44} & 2\tilde{c}_{45} & 2\tilde{c}_{46} \\ \sqrt{2}\,\tilde{c}_{51} & \sqrt{2}\,\tilde{c}_{52} & \sqrt{2}\,\tilde{c}_{53} & 2\tilde{c}_{54} & 2\tilde{c}_{55} & 2\tilde{c}_{56} \\ \sqrt{2}\,\tilde{c}_{61} & \sqrt{2}\,\tilde{c}_{62} & \sqrt{2}\,\tilde{c}_{63} & 2\tilde{c}_{64} & 2\tilde{c}_{65} & 2\tilde{c}_{66} \end{bmatrix} \begin{bmatrix} E_{11} \\ E_{22} \\ E_{33} \\ \sqrt{2}\,E_{13} \\ \sqrt{2}\,E_{23} \\ \sqrt{2}\,E_{12} \end{bmatrix}
\tag{B.4}
$$

The transformation of the three-dimensional second rank tensor components to six-dimensional vector components is directly assured by these relations and *vice versa*. In particular, it has been shown in (Mehrabadi and Cowin, 1990) that the 2 and square root factors introduced on some *moduli* of $\tilde{c}$ ensures that $\tilde{c}$ is a tensor in Euclidian six-dimensional space. In addition, the $\sqrt{2}$ factor on the vectors $\widetilde{\mathbf{S}}$ (whose the components are defined by $[S_{11}, S_{22}, S_{33}, \sqrt{2}\,S_{13}, \sqrt{2}\,S_{23}, \sqrt{2}\,S_{12}]$) or $\widetilde{\mathbf{E}}$ guarantees that the scalar product of the six dimensional vectors is equal to the trace of the product of the corresponding second rank tensors $\widetilde{\mathbf{S}} \cdot \widetilde{\mathbf{E}} = \mathrm{Tra}(\mathbf{S}^T \mathbf{E})$ where Tra and "T" are the trace and transposition operators, respectively.

In the text body, the notation tilde has been dropped.

C. Representation of classes of material symmetry

In this section, we resume the representation of the symmetry class of isotropic materials used (1) for describing the result of micro-mechanical homogenization and (2) for approaching the problem of the classification of the results of the FE and FFT methods. For a wider overview on other symmetry classes we refer to the works of (Walpole, 1984) and (Guilleminot and Soize, 2013). In our presentation, N_S represents the number of necessary and sufficient coefficients c_i and elements of the orthogonal base (but generally non orthonormal) $\{\mathbb{b}_i\}$ for the complete definition of a isotropic symmetry class, denoted by S. For instance $N_S = 5$ for a material in the *transverse isotropic* symmetry class, $N_S = 9$ for the *orthotropic* one and $N_S = 2$ for an *isotropic* one, and so on. This decomposition in the base is given by:

$$
\mathfrak{c}_S := \sum_{i=1}^{N_S} \mathfrak{c}_i\, \mathbb{b}_i .
\tag{C.1}
$$

C.1. Isotropic material

An isotropic material is completely defined by two coefficients c_1 and c_2 and its base:

$$
[\mathbb{b}_1]_{ijkl} = (1/3)\delta_{ij}\delta_{kl}
$$
$$
[\mathbb{b}_2]_{ijkl} = [\mathbb{i}]_{ijkl} - [\mathbb{b}_1]_{ijkl}
\tag{C.2}
$$

where $[\mathbb{i}]$ denotes the fourth-order symmetric identity tensor which is defined by the relation:

$$
[\mathbb{i}]_{ijkl} = 1/2(\delta_{ij}\delta_{kl} + \delta_{ik}\delta_{jl}),
$$

δ_{ij} designates the Kronecker's symbol.

The two coefficients c_1 and c_2 can be related with other couples of coefficients as Lamé coefficients, or in the alternative way with Young's *modulus* and Poisson's ratio, according well known functions. For instance, it results that $c_1 = 3 \times K$ and $c_2 = 2 \times G$ where K and G are respectively the bulk and shear *moduli*.

C.2. Transverse isotropic material

A transverse isotropic material is completely defined by the direction of its axe of symmetry, hereafter noted $\mathbf{e}_n$. Once $\mathbf{e}_n$ has been assigned, any transverse isotropic tensor is fully defined by:

$$
\begin{aligned}
\mathbf{p} &= \mathbf{e}_n \otimes \mathbf{e}_n, & \mathbb{b}_1 &= \mathbf{p} \otimes \mathbf{p}; \\
\mathbf{q} &= \mathbf{i} - \mathbf{p}, & \mathbb{b}_2 &= \mathbf{q} \otimes \mathbf{q}; \\
& & \mathbb{b}_3 &= \tfrac{1}{\sqrt{2}}(\mathbf{p} \otimes \mathbf{q} + \mathbf{q} \otimes \mathbf{p}); \\
& & \mathbb{b}_4 &= \mathbf{q} \boxtimes \mathbf{q} - \mathbb{b}_2; \\
& & \mathbb{b}_5 &= \mathbf{i} \boxtimes \mathbf{i} - \mathbb{b}_1 - \mathbb{b}_2 - \mathbb{b}_4;
\end{aligned}
\tag{C.3}
$$

where the $\mathbf{i}$ represents the identity tensor and the products $\otimes$ and $\boxtimes$ operate as:

$$
(g \otimes f)_{ij} = g_i f_j;
$$
$$
[\mathbf{p} \otimes \mathbf{q}]_{ijkl} = [\mathbf{p}]_{ij}[\mathbf{q}]_{kl};
$$
$$
[\mathbf{p} \boxtimes \mathbf{q}]_{ijkl} = \tfrac{1}{2}([\mathbf{p}]_{ik}[\mathbf{q}]_{jl} + [\mathbf{p}]_{il}[\mathbf{q}]_{jk}).
\tag{C.4}
$$

Throughout this work, the Haversian Porosity has been assumed to be aligned in the e_3 direction and the direction of the collagen molecules aligned to the direction of the HP. As consequence of the Mori-Tanaka scheme (MTs) of cylindrical inclusions in the $\mathbf{e}_3$ direction and the micro-mechanical model of the Ultra-Structure transverse isotropic in the direction $\mathbf{e}_n = \mathbf{e}_3$. For the same reason, the application of the MTs to the cylindrical pores and the ultrastructure matrix produce a transverse isotropic (in the $\mathbf{e}_n = \mathbf{e}_3$ direction) model of cortical bone.

We note TI($\mathbf{e}_n$) the set of elasticity tensors belonging to the symmetry transverse isotropic with axe $\mathbf{e}_n$.

C.3. Orthotropic material

An orthotropic material is defined as a function of an orthonormal base described from the 3 vectors **a**, **b** and **c**. The nine base-tensors of fourth-order are given as function of its axis of symmetry. The general representation is given by:

$$\mathbb{b}_1 = \mathbb{e}^{11}, \qquad \mathbb{e}^{11} = (\mathbf{a} \otimes \mathbf{a}) \otimes (\mathbf{a} \otimes \mathbf{a});$$
$$\mathbb{b}_2 = \mathbb{e}^{22} \qquad \mathbb{e}^{22} = (\mathbf{b} \otimes \mathbf{b}) \otimes (\mathbf{b} \otimes \mathbf{b});$$
$$\mathbb{b}_3 = \mathbb{e}^{33}, \qquad \mathbb{e}^{33} = (\mathbf{c} \otimes \mathbf{c}) \otimes (\mathbf{c} \otimes \mathbf{c});$$
$$\mathbb{b}_4 = \tfrac{1}{2}(\mathbb{e}^{12} + \mathbb{e}^{21}), \quad \mathbb{e}^{12} = (\mathbf{a} \otimes \mathbf{a}) \otimes (\mathbf{b} \otimes \mathbf{b})$$
$$\mathbb{e}^{21} = (\mathbf{b} \otimes \mathbf{b}) \otimes (\mathbf{a} \otimes \mathbf{a});$$
$$\mathbb{b}_5 = \tfrac{1}{2}(\mathbb{e}^{23} + \mathbb{e}^{32}), \quad \mathbb{e}^{23} = (\mathbf{b} \otimes \mathbf{b}) \otimes (\mathbf{c} \otimes \mathbf{c})$$
$$\mathbb{e}^{32} = (\mathbf{c} \otimes \mathbf{c}) \otimes (\mathbf{b} \otimes \mathbf{b});$$
$$\mathbb{b}_6 = \tfrac{1}{2}(\mathbb{e}^{13} + \mathbb{e}^{31}), \quad \mathbb{e}^{13} = (\mathbf{a} \otimes \mathbf{a}) \otimes (\mathbf{c} \otimes \mathbf{c})$$
$$\mathbb{e}^{31} = (\mathbf{c} \otimes \mathbf{c}) \otimes (\mathbf{a} \otimes \mathbf{a});$$
$$[\mathbb{b}_7]_{ijkl} = (a_i b_j + a_j b_i) \times (a_k b_l + a_l b_k);$$
$$[\mathbb{b}_8]_{ijkl} = (b_i c_j + b_j c_i) \times (b_k c_l + b_l c_k);$$
$$[\mathbb{b}_9]_{ijkl} = (a_i c_j + a_j c_i) \times (a_k c_l + a_l c_k). \tag{C.5}$$

where the used products are defined in Eq. (C.4). We denote by O the set of elasticity tensors belonging to the orthotropic symmetry class with respect to the axis (**a**, **b**, **c**). This class is denoted by O(**a**, **b**, **c**).

D. Jensen' inequality

Let X be a d-dimensional random vector, h a *convex* function (respectively *concave*), Y a random variable defined by the image of X through h (*i.e.* $Y = h(X)$), then:

$$h(\mathbb{E}(X)) \leq \mathbb{E}(Y) = \mathbb{E}(h(X)), \qquad (h(\mathbb{E}(X)) \geq \mathbb{E}(Y) = \mathbb{E}(h(X)), \tag{D.1}$$

where $\mathbb{E}(*)$ designates the mathematical expectation. For detail on the proof see (Jacod and Protter, 2003).

E. Tables E.8 and E.9

Table E.8
Estimation by FFT methods. Projection onto the transverse isotropic subspace TI($\mathbf{e}_n$).

FFT														
RVE	θ	z	%err.	c_1	c_2	c_3	c_4	c_5	Y_1	Y_3	G_{12}	G_{13}	ν_{12}	ν_{13}
#	[deg]	μm	[−]	[GPa]	[GPa]	[GPa]	[GPa]	[GPa]	[GPa]	[GPa]	[GPa]	[GPa]	[−]	[−]
1	− 40	550	0.80	17.951	20.779	9.887	7.980	8.397	10.50	13.25	3.99	4.20	0.32	0.27
2	− 40	450	2.38	15.684	17.861	8.790	6.235	6.822	8.41	11.36	3.12	3.41	0.35	0.26
3	− 40	350	0.79	15.492	18.029	8.928	6.305	6.746	8.47	11.07	3.15	3.37	0.34	0.27
4	− 40	250	1.71	14.178	17.075	8.650	5.811	5.987	7.79	9.80	2.91	2.99	0.34	0.28
5	− 40	150	1.33	13.140	15.642	8.146	4.904	5.153	6.70	8.90	2.45	2.58	0.37	0.28
6	− 30	550	3.64	14.744	16.990	8.458	5.754	6.193	7.81	10.53	2.88	3.10	0.36	0.26
7	− 30	450	1.16	15.787	18.078	8.928	6.337	6.763	8.53	11.38	3.17	3.38	0.35	0.26
8	− 30	350	0.99	15.253	18.147	9.028	6.490	6.743	8.61	10.76	3.25	3.37	0.33	0.28
9	− 30	250	1.05	14.663	17.467	8.826	6.111	6.211	8.13	10.20	3.06	3.11	0.33	0.28
10	− 30	150	0.61	13.229	15.980	8.365	5.069	5.178	6.88	8.85	2.53	2.59	0.36	0.29
11	− 20	550	2.64	15.407	17.243	8.584	5.812	6.215	7.93	11.13	2.91	3.11	0.36	0.25
12	− 20	450	2.48	14.789	17.152	8.614	5.919	6.138	7.96	10.46	2.96	3.07	0.34	0.27
13	− 20	350	1.13	13.429	15.997	8.275	5.087	5.332	6.94	9.15	2.54	2.67	0.36	0.28
14	− 20	250	2.13	13.119	15.678	8.186	4.889	5.157	6.69	8.85	2.44	2.58	0.37	0.28
15	− 20	150	0.99	12.204	14.705	7.887	4.235	4.367	5.88	7.97	2.12	2.18	0.39	0.28
16	− 10	550	2.84	15.437	17.784	8.805	6.150	6.551	8.30	11.08	3.07	3.28	0.35	0.26
17	− 10	450	2.23	14.598	17.057	8.588	5.764	6.113	7.79	10.27	2.88	3.06	0.35	0.27
18	− 10	350	1.56	14.103	16.407	8.370	5.338	5.638	7.28	9.83	2.67	2.82	0.36	0.27
19	− 10	250	2.79	12.481	14.684	7.763	4.253	4.520	5.94	8.38	2.13	2.26	0.40	0.27
20	− 10	150	1.40	12.569	15.230	8.105	4.523	4.622	6.23	8.26	2.26	2.31	0.38	0.28
21	0	550	12.22	12.914	13.412	7.027	3.479	4.259	5.11	9.23	1.74	2.13	0.47	0.20
22	0	450	3.04	14.077	16.203	8.200	5.279	5.638	7.22	9.93	2.64	2.82	0.37	0.26
23	0	350	1.16	14.226	16.794	8.558	5.494	5.856	7.47	9.87	2.75	2.93	0.36	0.27
24	0	250	2.99	12.753	14.940	7.881	4.351	4.710	6.08	8.60	2.18	2.36	0.40	0.26
25	0	150	1.76	11.788	13.895	7.531	3.701	3.936	5.26	7.71	1.85	1.97	0.42	0.26

26	10	550	2.22	16.214	18.645	9.122	6.706	7.131	8.96	11.75	3.35	3.57	0.34	0.26
27	10	450	2.40	15.080	17.400	8.664	5.903	6.384	8.00	10.77	2.95	3.19	0.36	0.26
28	10	350	1.90	13.584	15.996	8.196	5.177	5.505	7.05	9.39	2.59	2.75	0.36	0.27
29	10	250	2.70	12.482	14.789	7.820	4.333	4.720	6.03	8.35	2.17	2.36	0.39	0.27
30	10	150	2.11	11.949	14.169	7.605	3.981	4.199	5.58	7.87	1.99	2.10	0.40	0.27
31	20	550	2.38	15.945	17.775	8.974	6.290	6.687	8.42	11.41	3.14	3.34	0.34	0.26
32	20	450	2.53	15.085	16.962	8.454	5.624	6.250	7.70	10.87	2.81	3.12	0.37	0.25
33	20	350	2.34	16.318	18.915	9.227	6.893	7.289	9.17	11.82	3.45	3.64	0.33	0.27
34	20	250	1.24	14.275	16.933	8.509	5.741	5.989	7.74	10.00	2.87	2.99	0.35	0.27
35	20	150	3.38	11.809	13.160	7.083	3.281	3.701	4.80	8.00	1.64	1.85	0.46	0.23
μ	–	–	2.26	14.193	16.513	8.401	5.406	5.746	7.35	9.91	2.70	2.87	0.37	0.27

Table E.9
Estimation by FEM methods. Projection onto the transverse isotropic subspace TI($\mathbf{e}_n$).

FFT

RVE	θ	z	%err.	c_1	c_2	c_3	c_4	c_5	Y_1	Y_3	G_{12}	G_{13}	ν_{12}	ν_{13}
#	[deg]	μm	[−]	[GPa]	[GPa]	[GPa]	[GPa]	[GPa]	[GPa]	[GPa]	[GPa]	[GPa]	[−]	[−]
1	− 40	550	0.91	17.918	20.773	9.892	8.286	8.500	10.75	13.21	4.14	4.25	0.30	0.27
2	− 40	450	1.82	15.763	17.843	8.770	6.622	7.049	8.77	11.45	3.31	3.52	0.32	0.27
3	− 40	350	1.28	15.543	17.975	8.901	6.561	6.878	8.69	11.13	3.28	3.44	0.32	0.27
4	− 40	250	1.30	14.260	17.077	8.640	6.013	6.209	7.98	9.89	3.01	3.10	0.33	0.29
5	− 40	150	0.74	13.042	15.498	8.081	5.094	5.308	6.86	8.83	2.55	2.65	0.35	0.29
6	− 30	550	2.18	15.222	17.575	8.637	6.577	6.918	8.66	10.98	3.29	3.46	0.32	0.27
7	− 30	450	1.14	15.808	18.135	8.949	6.660	7.013	8.82	11.39	3.33	3.51	0.32	0.27
8	− 30	350	0.91	15.226	18.152	9.029	6.734	6.879	8.82	10.73	3.37	3.44	0.31	0.29
9	− 30	250	0.86	14.648	17.413	8.801	6.166	6.351	8.18	10.20	3.08	3.18	0.33	0.29
10	− 30	150	0.31	13.270	16.005	8.361	5.268	5.374	7.07	8.90	2.63	2.69	0.34	0.29
11	− 20	550	0.95	15.449	17.659	8.739	6.597	6.880	8.69	11.12	3.30	3.44	0.32	0.27
12	− 20	450	1.61	14.654	17.126	8.603	6.114	6.382	8.12	10.33	3.06	3.19	0.33	0.28
13	− 20	350	0.73	13.423	15.933	8.221	5.379	5.564	7.20	9.18	2.69	2.78	0.34	0.29
14	− 20	250	1.50	13.303	15.826	8.213	5.274	5.490	7.08	9.04	2.64	2.75	0.34	0.29
15	− 20	150	0.67	12.200	14.635	7.840	4.457	4.598	6.09	8.00	2.23	2.30	0.37	0.29
16	− 10	550	1.70	15.658	18.121	8.917	6.809	7.054	8.95	11.27	3.40	3.53	0.31	0.28
17	− 10	450	1.68	14.591	17.037	8.567	6.027	6.316	8.03	10.28	3.01	3.16	0.33	0.28
18	− 10	350	1.58	14.090	16.518	8.409	5.820	6.011	7.73	9.81	2.91	3.01	0.33	0.28
19	− 10	250	1.41	12.659	14.979	7.844	4.867	5.049	6.57	8.55	2.43	2.52	0.35	0.28
20	− 10	150	0.86	12.616	15.253	8.087	4.800	4.878	6.50	8.33	2.40	2.44	0.35	0.29
21	0	550	5.20	12.987	14.215	7.337	5.035	5.451	6.71	9.20	2.52	2.73	0.33	0.27
22	0	450	2.13	14.168	16.308	8.226	5.743	6.069	7.67	10.02	2.87	3.03	0.34	0.27
23	0	350	0.58	14.283	16.843	8.530	5.937	6.161	7.89	9.96	2.97	3.08	0.33	0.28
24	0	250	2.24	12.777	14.842	7.817	4.620	4.934	6.33	8.66	2.31	2.47	0.37	0.27
25	0	150	1.17	12.137	14.232	7.591	4.365	4.602	5.98	8.09	2.18	2.30	0.37	0.28
26	10	550	1.62	16.391	18.901	9.209	7.214	7.506	9.46	11.90	3.61	3.75	0.31	0.27
27	10	450	1.50	15.176	17.659	8.760	6.565	6.828	8.63	10.83	3.28	3.41	0.31	0.28
28	10	350	1.58	13.663	16.098	8.231	5.586	5.817	7.44	9.45	2.79	2.91	0.33	0.28
29	10	250	1.11	12.689	15.088	7.887	4.936	5.159	6.65	8.57	2.47	2.58	0.35	0.29
30	10	150	1.21	11.961	14.213	7.607	4.362	4.551	5.95	7.89	2.18	2.28	0.36	0.29
31	20	550	1.86	15.705	17.856	8.820	6.523	6.924	8.67	11.35	3.26	3.46	0.33	0.27
32	20	450	1.79	15.293	17.241	8.539	6.302	6.728	8.37	11.06	3.15	3.36	0.33	0.27
33	20	350	1.92	16.016	18.558	9.102	6.999	7.294	9.19	11.55	3.50	3.65	0.31	0.28
34	20	250	0.97	14.166	16.691	8.423	5.920	6.170	7.86	9.92	2.96	3.08	0.33	0.28
35	20	150	3.45	12.077	13.850	7.323	4.430	4.718	6.02	8.20	2.21	2.36	0.36	0.27
μ	–	–	1.50	14.252	16.632	8.426	5.847	6.103	7.78	9.98	2.92	3.05	0.33	0.28

References

Apostol, L., Boudousq, V., Basset, O., Odet, C., Yot, S., Tabary, J., Dinten, J.M., Boiler, E., Kotzki, P.O., Peyrin, F., 2006. Relevance of 2d radiographic texture analysis for the assessment of 3d bone micro-architecture. Med. Phys. 33 (9), 3546–3556.

Barkaoui, A., Hambli, R., 2011. Finite element 3d modeling of mechanical behavior of mineralized collagen microfibrils. J. Appl. Biomater. Biomech. 9 (3), 199–205.

Barkaoui, A., Hambli, R., 2014. Nanomechanical properties of mineralised collagen microfibrils based on finite elements method: biomechanical role of cross-links. Comput. Meth. Biomech. Biomed. Eng. 17 (4), 1590–1601.

Brisard, B., Dormieux, L., 2010. FFT-based methods for the mechanics of composites: a general variational framework. Comput. Mater. Sci. 49 (3).

Broz, J.J., Simske, S.J., Greenberg, A.R., 1995. Material and compositional properties of selectively demineralised cortical bone. J. Biomech. 28 (11), 1357–1368.

Burghardt, A.J., Link, T.M., Majumdar, S., 2011. High-resolution computed tomography for clinical imaging of bone microarchitecture. Clin. Orthop. Relat. Res. 469 (8), 2179–2193.

Ciarlet, P.G., 1989. Introduction to Numerical Linear Algebra and Optimisation. Cambridge University Press, Cambridge.

COMSOL Multiphysics. version 5.2. COMSOL, Inc., Paris, France, 2015.

Cowin, S.C., 2001. Bone Mechanics Handbook. Taylor and Francis.

Crolet, J.M., Aoubiza, B., Meunier, A., 1993. Compact bone: numerical simulation of mechanical characteristics. J. Biomech. 26 (6), 677–687.

Devroye, L., 1986. Non Uniform Random Variate Generation. Springer Verlag, New York.

Eshelby, J.D., 1957. The determination of the elastic field of an ellipsoidal inclusion, and a related problems. Proc. Roy. Soc. Lond. 241 (1226), 376–396.

Fritsch, A., Hellmich, C., 2007. Universal microstructural patterns in cortical and trabecular, extracellular and extravascular bone materials: micromechanics-based prediction of anisotropic elasticity. J. Theor. Biol. 244 (4), 597–620.

Granke, M., Grimal, Q., Parnell, W.J., Raum, K., Gerisch, A., Peyrin, F., Saï, A., Laugier, P., 2015. To what extent can cortical bone millimeter-scale elasticity be predicted by a two-phase composite model with variable porosity? Acta Biomater. 12, 207–215.

Guilleminot, J., Soize, C., 2013. On the statistical dependence for the components of random elasticity tensors exhibiting material symmetry properties. J. Elasticity 111 (2), 883–901.

Hellmich, C., Ulm, F.J., 2002. Micromechanical model for ultrastructural stiffness of mineralized tissues. J. Eng. Mech. 128, 898–908.

Hellmich, C., Barthelemy, J., Dormieux, L., 2004a. Mineral-collagen interactions in elasticity of bone ultrastructure - a continuum micromechanics approach. Eur. J. Mech. Solid. 23, 783–810.

Hellmich, C., Ulm, F.J., Dormieux, L., 2004b. Can the diverse elastic properties of trabecular and cortical bone be attributed to only a few tissue-independent phase properties and their interactions? arguments from a multiscale approach. Biomech. Model. Mechanobiol. 2 (4), 219–238.

Jacod, J., Protter, P.E., 2003. Probability Essentials. Springer Science & Business Media.

Jaynes, E.T., 1957a. Information theory and statistical mechanics. Phys. Rev. 106 (4), 620–630.

Jaynes, E.T., 1957b. Information theory and statistical mechanics. Phys. Rev. 108 (2), 171–190.

Langer, M., Pacureanu, A., Suhonen, H., Grimal, Q., Cloetens, P., Peyrin, F., 2012. X-ray phase nanotomography resolves the 3d human bone ultrastructure. PLoS One 7 (8), e35691.

Laws, N., 1977. The determination of stress and strain concentrations at an ellipsoidal inclusion in an anisotropic material. J. Elasticity 7 (1), 91–97.

Laws, N., 1985. A note on penny-shaped cracks in transversely isotropic materials. Mech.

Mater. 4 (2), 209–212.

Mehrabadi, M.M., Cowin, S.C., 1990. Eigentensors of linear anisotropic elastic materials. Q. J. Mech. Appl. Math. 43 (1), 15–41.

Monchiet, V., 2015. Combining FFT methods and standard variational principles to compute bounds and estimates for the properties of elastic composites. Comput. Meth. Appl. Mech. Eng. 283, 454–473.

Monchiet, V., Bonnet, G., 2012. A polarization-based FFT iterative scheme for computing the effective properties of elastic composites with arbitrary contrast. Int. J. Numer. Meth. Eng. 89 (11), 1419–1436.

Moulinec, H., Suquet, P., 1998. A numerical method for computing the overall response of nonlinear composites with complex microstructure. Comput. Meth. Appl. Mech. Eng. 157, 69–94.

Nemat-Nasser, S., Hori, M., 1999. Micromechanis: Overall Properties of Heterogeneous Materials, second ed. Applied Mathematics and Mechanics, North-Holland.

Nuzzo, S., Peyrin, F., Cloetens, P., Baruchel, J., Boivin, G., 2002. Quantification of the degree of mineralization of bone in three dimensions using synchrotron radiation microtomography. Med. Phys. 29 (11), 2672–2681.

Parnell, W.J., Vu, M.B., Grimal, Q., Naili, S., 2011. Analytical methods to determine the effective mesoscopic and macroscopic elastic properties of cortical bone. Biomech. Model. Mechanobiol. 39 (21), 5659–5678.

Podio-Guidugli, P., 2000. A Primer in Elasticity, vol. 58 Kluwer Academic Publishers.

Racila, M., Crolet, J.M., 2007. Nano and macro structure of cortical bone: numerical investigations. Mech. Adv. Mater. Struct. 14 (8), 655–663.

Raum, K., Cleveland, O., Peyrin, F., Laugier, P., 2006. Derivation of elastic stiffness from site-matched mineral density by acoustic impedance map. Phys. Med. Biol. 51, 747–758.

Rohan, E., Naili, S., Cimrman, R., Lemaire, T., 2012. Multiscale modeling of a fluid saturated medium with double porosity: relevance to the compact bone. J. Mech. Phys. Solid. 60 (5), 857–881.

Ruffoni, D., Fratzl, P., Roschger, P., Klaushofer, K., Weinkamer, R., 2007. Bone mineralization density distribution as a fingerprint of the mineralization process. Bone 40, 1308–1319.

Sansalone, V., Naili, S., Bousson, V., Bergot, C., Peyrin, F., Laredo, J.D., Haiat, G., 2010. Determination of the heterogeneous anisotropic elastic properties of human femoral bone: from nanoscopic to organ scale. J. Biomech. 43 (10), 1857–1863.

Sansalone, V., Naili, S., Desceliers, C., 2014. A stochastic homogenization approach to estimate bone elastic properties. Compt. Rendus Mec. 342 (5), 326–333.

Sansalone, V., Gagliardi, D., Desceliers, C., Bousson, V., Laredo, J.D., Peyrin, F., Haiat, G., Naili, S., 2016. Stochastic multiscale modelling of cortical bone elasticity based on high-resolution imaging. Biomechanics Model. Mechanobiol. 15 (1), 111–131.

Shannon, C., 1948. A mathematical theory of communication. Tech. J. 27 Bell Syst.

Simpleware 5.0 ScanIP+. version 5.0. Simpleware Ltd, Exeter, UK, 2012.

Soize, C., 2001. Maximum entropy approach for modeling random uncertainties in transient elastodynamics. J. Acoust. Soc. Am. 109 (5), 1979–1996.

Soize, C., 2004. Probabilités et Modélisation des incertitudes. Eléments de base et concepts fondamentaux. Lecture notes. Université Pars-Est Marne la Vallée.

Suquet, P. (Ed.), 1997. Continuum Micromechanics. Springer-Verlag, Wien Number 377 in CISM Lecture Notes.

Suvorov, A., Dvorak, G., 2002. Rate form of the eshelby and hill tensors. Int. J. Solid Struct. 39, 5659–5678.

Walpole, L.J., 1984. Fourth-rank tensors of the thirty-two crystal classes: multiplication tables. Proc. Royal Soc. Lond. Serie A 391, 149–179.

Zaoui, A., 2002. Continuum micromechanics: survey. J. Eng. Mech. 128 (8), 808–816.

Zohdi, T.I., Wriggers, P., 2001. Computational micro-macro material testing. Arch. Comput. Meth. Eng. 8 (2), 131–228.